Comparison of Strain Gage and Fiber Optic Sensors On A Sting Balance In A Supersonic Wind Tunnel

By

Alex T. Edwards

Thesis submitted to the faculty of the
Virginia Polytechnic Institute and State University
in partial fulfillment of the requirements for the degree of
MASTER OF SCIENCE
in
Aerospace Engineering

APPROVED BY:
Dr. Joseph A. Schetz, Chairman
Dr. Rakesh K. Kapania
Dr. Wade J. Pulliam

December 2000
Blacksburg, Virginia

Keywords: Fiber optic sensors, strain gage sensors, sting balance, aerodynamic forces and moments, supersonic, wind tunnel testing

Comparison of Strain Gage and Fiber Optic Sensors On A Sting Balance In A Supersonic Wind Tunnel

by

Alex T. Edwards

Abstract

Force and moment balances have proved to be essential in the measurement and calculation of aerodynamic properties during wind tunnel testing. With the recent advancements of technology, new fiber optic sensors have been designed to replace the conventional foil strain gage sensors commonly found on balances, thereby offering several distinct advantages. The use of fiber optic sensors on a balance brings with it some potential advantages over conventional strain gage balances including increased resolution and accuracy, insensitivity to electromagnetic interference, and the capability of use at high temperatures. By using the fiber optic sensors, some of the limitations of the conventional balance can be overcome, leading to a better overall balance design.

This thesis considers an initial trial application of new fiber optic sensors on a conventional, six-component sting balance while retaining the original foil strain gage sensors for comparison. Tests were conducted with a blunt, 10º half-angle cone model in the Virginia Tech 9x9 inch Supersonic Wind Tunnel at Mach 2.4 with a total pressure of 48 psia and ambient total temperature of 25.3ºC. Results showed a close comparison between the foil strain gages and the fiber optic sensor measurements, which were set up to measure the normal force and pitching moment on the blunt cone model. A Finite Element Model (FEM) of the sting balance was produced in order to determine the best locations for the fiber optic sensors on the sting balance. Computational Fluid Dynamics (CFD) was also used in order to predict and compare the results acquired from all of the sensors.

Acknowledgments

I would first like to thank the AOE faculty and staff for all their hard work and dedication in helping make the Aerospace Department at Virginia Tech nationally recognized. Reaching #10 in U.S. News and World Report Top 20 Aerospace Graduate Schools is a great achievement and I'm sure with the current research being conducted at Virginia Tech, we will proceed up the ranks well within the Top 10.

Most notably, I would like to thank my advisor, Dr. Schetz, for providing me with this great research opportunity and for providing me with the experience necessary for a credible entry into the aerospace industry. The other members who reside on my committee also deserve due recognition for their support and guidance through these final efforts in completing my Master's Degree. Thank you Dr. Rakesh Kapania, Dr. Wade Pulliam, and Jason Borinski.

On the personal side of things, many close loved ones have also contributed to my success in life. First of all, thank you to my parents for "forcing" me to think about what I wanted to do in my now present future and then helping me get there both financially and physically. My fellow siblings, Justin, Marcus and Vicky, also deserve praise for many reasons, especially for helping me to relax during the demanding journey through the College of Engineering. Whatever y'all did, you helped me fulfill many aspects of my life. Finally, I must thank my girlfriend Amy Benedict. Her unwavering support was crucial to my success in graduate school.

Table of Contents

List of Figures

List of Tables

Chapter 1 – Introduction/Overview

The field of measurement and instrumentation has expanded rapidly in recent years. With the start of the 21st century, the need for high quality sensors to be integrated into sophisticated measurement and control systems is clear. Conventional metal foil strain gage sensors are used extensively in many engineering fields in order to measure such characteristics as stress, strain, forces and moments. In particular, the aerospace engineering field uses these strain gage sensors for structural analysis and to measure stability, control, and drag parameters with force and moment balances during wind tunnel testing.

The advent of fiber optic sensors is currently reaching new heights, yielding new sensors with potential advantages over conventional electrical based strain gage sensors such as higher resolution and accuracy, insensitivity to electromagnetic interference, and use in high temperature regimes. In this work, we study an initial trial application of fiber optic sensors placed on a wind tunnel sting balance while retaining the original foil strain gages for comparison.

1.1 Force and Moment Balances

Balances are commonly used for the measurement of aerodynamic loads associated with wind tunnel testing. Two fundamental types of balances are in use today: external balances, which carry the loads outside the tunnel before they are measured, and internal balances, which fit into the model and are arranged to send data out through electrical wires.[1] An internal balance is a carefully designed and precisely machined cantilever beam of complicated cross-section that is normally equipped with electrical-resistance strain-gage sensors. This type of internal balance is most commonly known in the aerodynamic field as a sting balance. The test model is mounted on a relatively long and slender sting that protrudes out from the aft end of the model. Sting mounting can become complicated when performing supersonic tests due to the inherently small cross

section of supersonic tunnels. This results in major restrictions on the size of the model and generates problems when fitting the balance inside the test model.

Wind tunnel testing requires a balance system capable of accurately measuring the forces and moments associated with the longitudinal and lateral stability and control of the given test model. Some important factors that must be taken into consideration during this selection process are the number and arrangement of the strain gages on the internal sting balance. When this selection process is complete, three types of balances are most commonly developed including a moment balance, a force balance, and a direct read force-moment balance.

1.1.1 Design of a Six-Component Strain Gage Balance

The balance used in conjunction with this research project is a six-component moment balance designed and developed by Arnold Engineering Development Center (AEDC) and is designated as Balance ID 8106 (4.00-Y-36-081). The sting balance can be seen in Figure 1.1. The resistance-wire strain gages are mounted to the balance to measure the bending moment at two points. These bending moments are designed to measure the pitching moment at two separate locations. By knowing the distance between the two moment arms, it is possible to reduce the pitching moment data and calculate the normal force, N. In Equation 1.1, M_b and M_a are the associated pitching moments and Δx is the distance between the two moment bridges. The overall pitching moment can be determined by referencing either of the two pitching moments to a specified point. A visual description of the normal force calculation is provided in Figure 1.2.

$$N = (M_b - M_a)/(\Delta x) \tag{1.1}$$

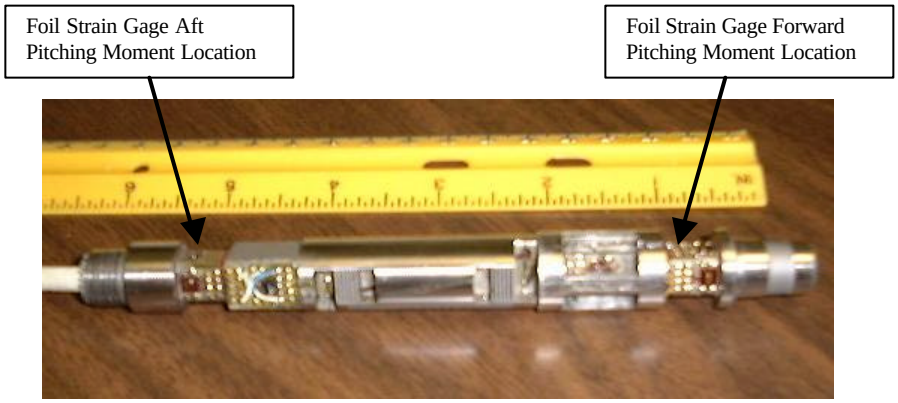

Figure 1.1 - Six-Component AEDC Sting Moment Balance

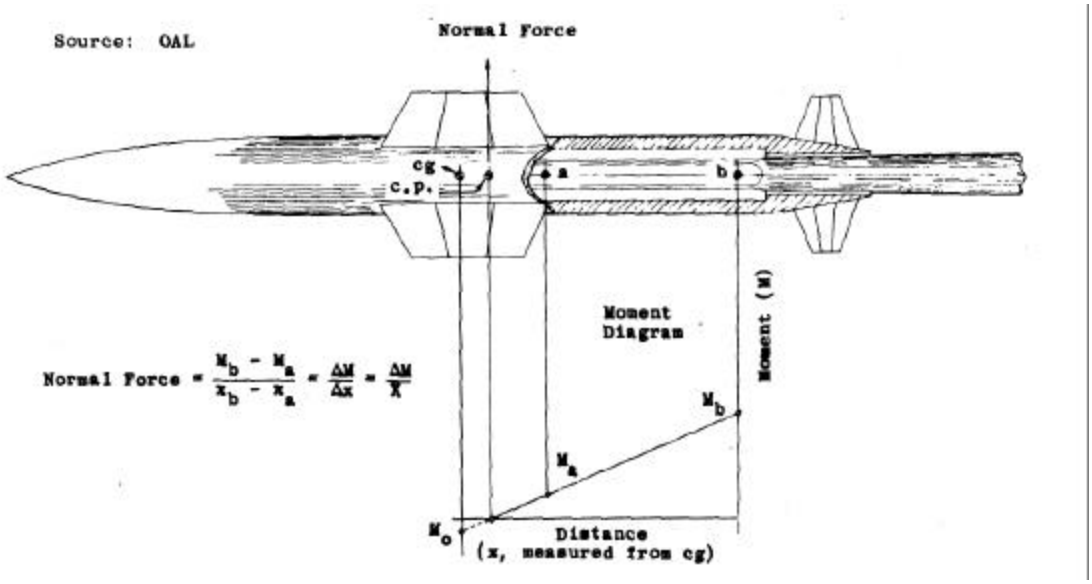

Figure 1.2 – Visual Reference for Normal Force Calculation[2]

In the same manner, strain gages mounted on the beam at 90 degrees to locations a and b measure the yawing moment. Therefore, calculation of the side force is also possible.

Now we have derived ways to calculate four components: normal force, side force, pitching moment, and yawing moment. The two components left to measure through the six-component sting balance are axial force (drag) and rolling moment. The

measurement of these quantities is somewhat unique and requires a detailed discussion. Since the fiber optics will not be set up on the balance to measure and compare these quantities in this work, they will not be discussed further here. The interested reader can find further detailed information on the measurement of these quantities in NAVORD Report 1488, Section 3.2.

1.1.2 Calibration of the Six-Component Strain Gage Balance

All devices that are to be used for measurement require a calibration so that the output can be converted to conventional units of measurement. In this case, the output from the conventional strain gages will be read through a data acquisition board directly into the computer and will be in units of voltage. These voltage readings must be further converted into the conventional units of forces and moments, which in this case will be pounds for force calculations and inch-pounds for pitching moment calculations. Of all the phases that a balance goes through when preparing for use in a tunnel, this calibration process is one of the most important. Many setups are possible to achieve accurate calibration results, but these setups are often very complicated and expensive to produce. An example of a calibration rig can be seen below in Figure 1.3.

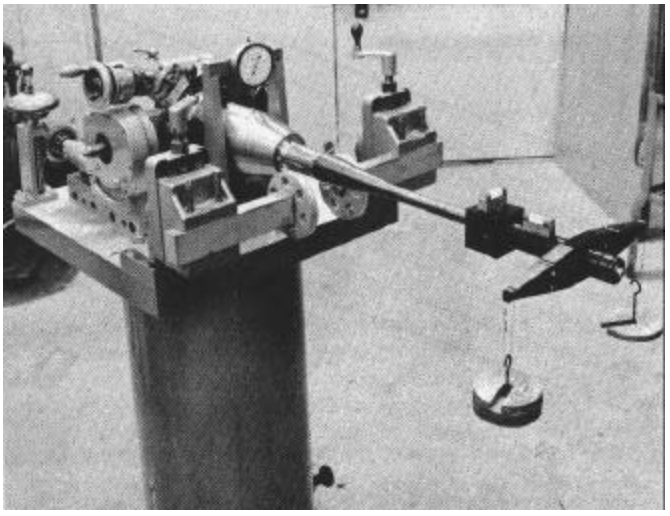

Figure 1.3 – Example Calibration Rig Setup[1]

The force and moment data obtained from any balance are no better than the calibration. Therefore, extreme care should be followed during the calibration process. For sake of discussion, please note that the loads applied during the loading session are classified as primary and secondary loads. The primary load is one that is changed incrementally and only loads one component on the balance at one time. The position and magnitude of this load must be accurately known in order that the effect of the incremental changes on the balance may be determined accurately. This process allows the determination of the linear first order primary sensitivities, which can also be understood as a scale factor for the conversion from volts to the conventional units being used.

The secondary load is one that remains constant during the period the primary load is being incrementally changed. This may load one or more balance components at a time. During this loading, the magnitude and position of the secondary load must remain constant as the primary load is changed. This allows one to determine the non-linear, second order interaction terms.

The interaction terms result from a certain load unintentionally affecting the non-targeted gage sensor. For example, when a normal force is applied directly to the balance, the two gages measuring the pitching moments will be directly affected by changing the voltage through the sensors. Unfortunately, this will also cause a small yet noticeable change in the voltage across the sensors intended to read only yawing moments. To avoid this, major improvements have been made to sting balances through careful engineering design and precise machining, but complete elimination of these effects is impossible and can only be minimized.

Overall, the painstaking calibration process can take weeks to achieve accurate results. Therefore, the manufacturer of the internal sting balance often completes this process. In this case, Arnold Engineering Development Center provided the matrix equations to help reduce the data from the strain gages. This includes both the primary sensitivities and the interaction matrix for all six components. All the constants in these equations were generated by a least squares fit of applied loads along with calibration equipment tares as

a function of gage readings and cross products (V(J)). In matrix form, the data reduction equation is provided in Equation 1.2 where N=1,6 and J=1,35.

$$[BC(N)] = [K(N)] * [D(N,J)] * [V(J)] \quad (1.2)$$

Balance Components	Primary Sensitivities	Interaction Matrix	Gage Readings
6X1	6X6	6X35	35X1
(calculated)	(constant)	(constant)	(gage output)

1.2 Conventional Strain Gage Sensors

There are several methods for measuring forces and moments electrically; most of them rely on amplifying the effect that small deflections have on the resistance, inductance or capacitance of the system[1]. Usually, the wire gage consists of a resistance made of very fine wire securely bonded to the member to be strained, in our case the balance. When a force is applied to the balance, the wire then becomes either in tension or compression. The resistance change of a wire when a force is applied is due in part to a change in length and cross-section, and in part to an actual change in specific resistance[2].

1.2.1 Theory and Instrumentation

The theory behind resistance-based sensors is relatively simple. All electrical components demonstrate some resistance to the flow of electricity, which can be measured by electronic instrumentation such as a multimeter. The electrical resistance strain gage is a strain-sensitive component bonded to the surface of a balance to measure strain. Foil gages, as used on balances, are mounted using a very thin lacquer layer having excellent mechanical and electrical properties. This helps improve the gage performance and stability. When the strain gage is stretched (or strained), its resistance changes in direct proportion to the strain. By measuring this change in electrical resistance, the strain is also known. Figure 1.4 displays a generalized setup for a typical strain gage with a force, F, applied to the arm.

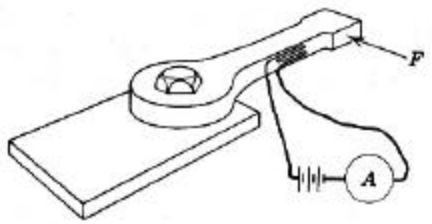

Figure 1.4 - Fundamental Strain Gage Setup

The gage factor, K, of a strain gage, relates the change in resistance (ΔR) to the change in length (ΔL). The gage factor is constant for a given strain gage, and R is the non-deformed resistance of the strain gage, so

$$K = (\Delta R/R)/ (\Delta L/L)= (\Delta R/R)/\varepsilon \qquad (1.3)$$

If the gage factor were due entirely to dimensional change, Poisson's ratio would suggest that the gage factor for any wire would be approximately 1.7. However, hundreds of different types of strain gages with different gage factors are commercially available, each having been developed in response to a demand for a gage to meet or withstand specific conditions. By rearranging the terms in Equation 1.3, we arrive at the equation for strain, ε.

$$\varepsilon=(\Delta R/R)/K \qquad (1.4)$$

1.2.2 Wheatstone Bridge

Wheatstone bridges are commonly used with strain gage setups to allow easier measurement of the small changes in resistance. In addition, Wheatstone bridges are inherently insensitive to supply-voltage fluctuations. Figure 1.5 shows a typical Wheatstone bridge circuit, which can be described as a null-measurement system.

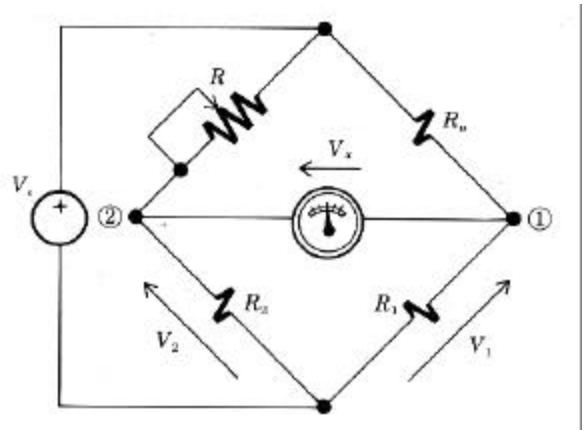

Figure 1.5 - Full Wheatstone Bridge Circuit

A null-measurement system differs from direct measurements in that the quantity being measured is compared with a known reference quantity. This strategy avoids unwanted interaction effects and usually results in greater precision than direct measurement, which depend on the accuracy of a meter movement.[3] The Wheatstone bridge circuit is designed for precise measurement of an unknown resistance R_u and utilizes a calibrated potentiometer R plus two known resistances R_1 and R_2. The resistance of R can be adjusted until the bridge is balanced with $V_x = 0$.

The circuit can be shown mathematically as

$$V_1=((R_1)/(R_1+R))*V_s \quad (1.5)$$

$$V_2=((R_2)/(R_2+R_u))*V_s \quad (1.6)$$

Since $V_x = V_2-V_1 =0$, we find that $V_2 = V_1$ and hence,

$$R_u=(R_2/R_1)*R \quad (1.7)$$

which is independent of the voltage source, V_s.[3]

The main advantage of this circuit over using a single strain gage is that some of the error sources (such as temperature dependence) will cancel each other out. The simplicity and broad frequency application, as well as it's outstanding capability for measuring changes in resistance as small as 0.001 ohms have justified the use of the Wheatstone bridge.[2]

1.2.3 Advantages and Disadvantages of Foil Strain Gages

Apart from the hundreds of applications strain gages can be used for, strain gages have other advantages at the most basic level. First, the construction and operation of these gages are very simple, yet they are so precise that strains on the order of 0.001% may be measured. Even the size of the gage can be seen as a huge advantage, roughly represented by the size and weight of a postage stamp, although many are much smaller. This permits strain gages to be applied and used on objects with small surface areas.

Although these advantages are highly regarded, some disadvantages of the strain gage must not be overlooked. The use of strain gages to measure aerodynamic loads on sting balances during wind tunnel testing has been so successful that it has promoted the need for a critical examination of the characteristics of the strain gage itself.[2]

The gages are subjected to the ambient stream conditions during wind tunnel testing both directly and indirectly through the supporting sting. The major source of error comes from the fact that the resistances of most wires change with temperature. This is one major reason why the Wheatstone bridge circuit was developed. Experiments have proven that temperature differentials on a sting, after thermal equilibrium has been reached during testing, are not normally large enough to introduce appreciable errors. Problems also arise in strain gages when the wind tunnel is operated at high temperatures. The bonding agent used to attach the sensor to the specimen often limits the maximum working temperature of the gage.

Another important disadvantage is the sensitivity of foil strain gages to electromagnetic interference (EMI). The operating principles behind the electrical-based strain gage sensors prove that this type of interference could be a problem during wind tunnel testing. The operation of these sensors near any EMI inducing equipment, such as a motor or plasma torch, can severely limit or hinder the strain gage results.

Another source of error that must be discussed is due to strain-gage creep. Experiments have shown that if a test element is subjected to a suddenly applied load, the strain-gage bridge output decreases with time from an initial value.[2] The rate of decrease is relatively large for the first few seconds and decreases thereafter so that the output approaches a constant asymptotic value. "This phenomenon is known as creep effect. The magnitude of the total change with time has been found to be approximately proportional to the unit strain of the material to which the gage is bonded when subjected to the applied load."[2] Apparently, the creep effect is the result of a partial relaxation of the bonding material.

1.3 Fiber Optic Sensors

The technology and the demand for fiber optics are firmly in place today. The diversity for which fiber optics may be used ranges anywhere from high-speed data transmission and imaging to use in biomedical systems and industrial process control. Many of the uses incorporate the need for sensors to measure specific quantities. Currently, up to 60 different parameters can be measured using fiber optic sensors including such quantities as temperature, pressure and strain.[4]

1.3.1 Fiber Optic Sensor Design

In an optical fiber, light is injected and then guided by a dielectric cylindrical core surrounded by a dielectric cladding. In basic terms, one can think of the light transmitted down the fiber as being reflected at the core/cladding interface. According to Snell's Law, this reflection is dependent on an angle derived as a function of the index ratio called the critical angle.[5]When the critical angle is not exceeded, the light will reflect and remain confined inside the core of the optical fiber. But, if the critical angle is exceeded, the light will not reflect, and it will therefore be lost and absorbed into the cladding. Overall, the fibers purpose is to act as a waveguide for the light and its inherent energy. Although a variety of fiber optic sensing techniques have been put to practical use in the last two decades, one of the most versatile techniques for fiber optic sensor applications

is Extrinsic Fabry-Perot Interferometry (EFPI). EFPI-based sensors incorporate the measurement of a distance across a cavity based on the formation of a low-finesse Fabry-Perot cavity. This cavity is placed between the polished end face of a fiber and a reflective surface, as shown schematically in Figure 1.6. As light is passed through the fiber, a portion of the light is reflected at the fiber/air interface, labeled R_1. The rest of the light continues along the optical path through the Fabry-Perot cavity and is reflected back into the fiber, shown as R_2.

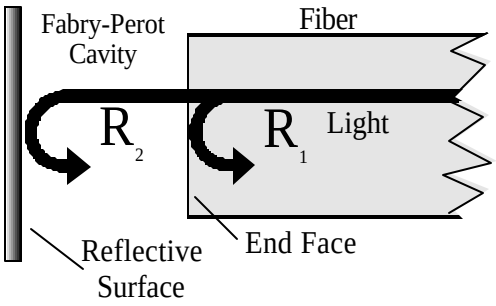

Figure 1.6 - Extrinsic Fabry-Perot Interferometer Concept

The two light waves, R_1 and R_2, proceed to interfere with each other, either constructively or destructively based on the difference in optical path lengths traveled by each light wave and their corresponding wavelength. The optical path length (OPL) represents the distance that light travels across the Fabry-Perot cavity. As shown in Equation 1.8, this length is a function of the index of refraction, n, and is therefore greatly dependent on the medium through which the light source travels. Since n~1.0 for air, the OPL is basically equal to the physical gap representing the distance from the reflector to the polished end of the fiber. Thus, it can act as a strain sensor.

$$OPL = Gap*n \tag{1.8}$$

In essence, the interaction between the two light waves in the Fabry-Perot cavity is modulated by a change in the index of refraction or a change in the physical gap distance. The ensuing light signal then travels back through the fiber to a detector where it is

converted into an electrical signal. This electrical signal is then demodulated by a signal processing system to produce a distance measurement.[5] The processing systems used in this experiment were all developed at Luna Innovations, a commercial fiber optic sensing company that sponsored and assisted in this work.

1.3.2 The Demodulation System

There are several methods that can be used for demodulating the signals from an EFPI cavity including: intensity-based and spectral interrogation systems. Spectral interrogation, otherwise known as white-light interferometry, is the method used for this study. White-light interferometry is an optical cross-correlation technique with the capability of precisely determining the path imbalance between two arms of an interferometer.[5] As used with the EFPI sensor, white–light interferometric methods provide the exact optical path length between the two end faces of the fiber. As previously mentioned, this region between the two fiber end faces is known as the Fabry-Perot cavity. Figure 1.7 below shows the basic configuration of the spectral interferometric sensing system.

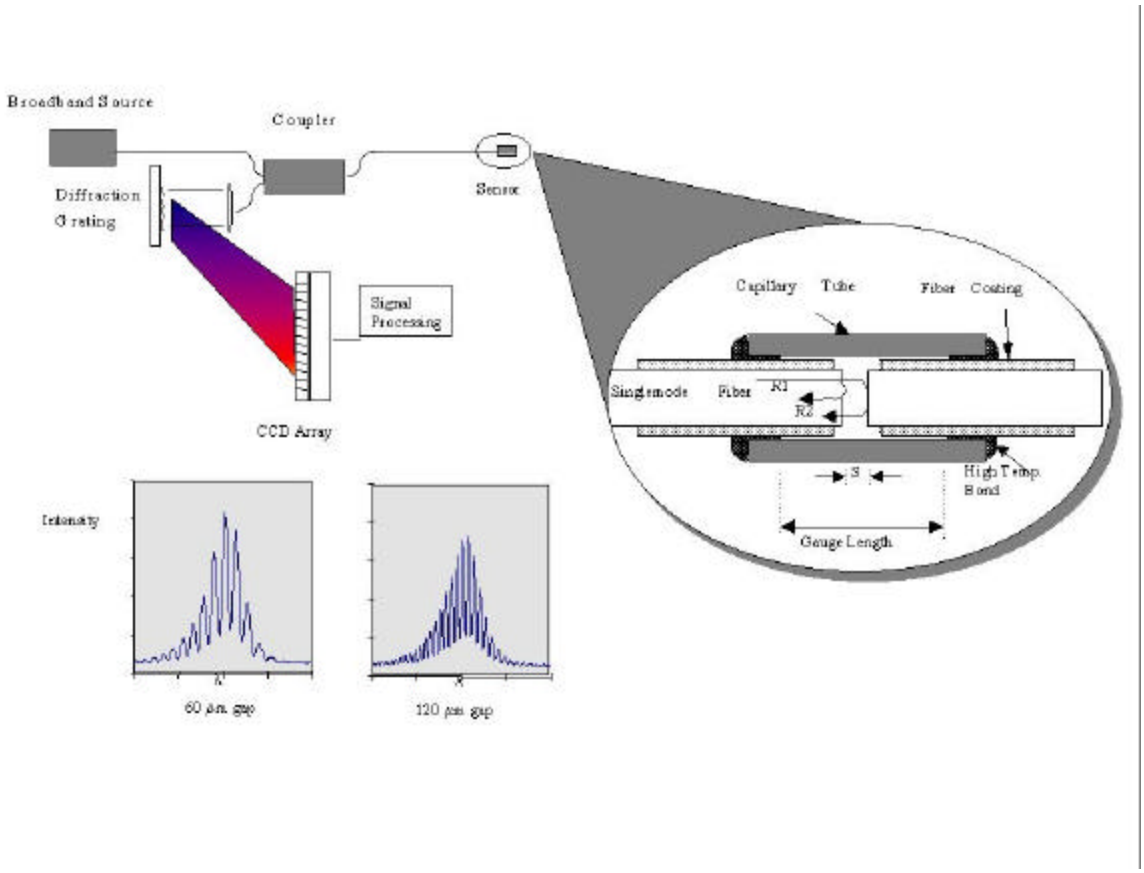

Figure 1.7 - Spectral Interferometric Sensing System

Although the software and hardware details of the fiber optic signal processing system are proprietary to Luna Innovations, Inc., a general description may be provided. As shown in the upper left of Figure 1.7, a broadband, white light source is transmitted to the fiber optic sensor, where it becomes modulated by the Fabry-Perot cavity. The modulated spectrum is then split into its wavelength components by a diffraction grating. These readings are then measured by a charged-coupled device (CCD) array. The spectrum produced is then taken from the CCD array and used in conjunction with the Luna Innovations algorithm to calculate the optical path length. The main part of the algorithm is a Fourier analysis, which transforms the signal from a wavelength to a gap. Although the output of this algorithm has numerous peaks, as seen in Figure 1.8, a peak search is used to determine the location of the maximum of the main peak, which is the absolute optical gap of the EFPI cavity.[6]

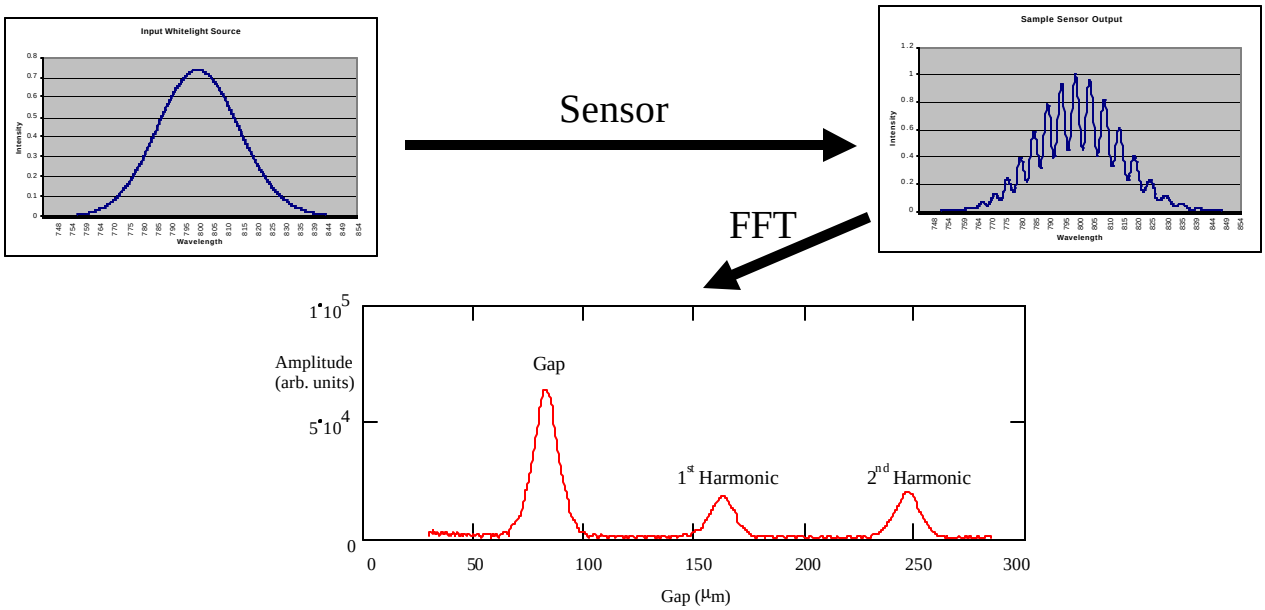

Figure 1.8 - Depiction of Spectral Interrogation System Method

Since the spectral interrogation system is gathering data from a range of wavelengths, the resolution and accuracy of the system is particularly impressive. Yet, there are some drawbacks that can affect measurements in wind tunnel environments. The main weakness is the speed of the system, which operates at 66 Hz. This is a problem in that many of the dynamic responses encountered in wind tunnel testing occur faster, even reaching into the hundreds of kilohertz category. The source of this problem is the speed of the internal spectrometer, which uses a CCD array to measure the intensities of the wavelengths.[5] The CCD array requires a certain integration time necessary for the pixels to receive enough light to create a charge later read by the A/D converters. Concurrently, the measurements from the sensor will be changing during this integration period, thereby preventing a clean signal from reaching the A/D converter. This problem is termed spectral "smearing".

Another problem with the spectral interrogation system is that it is more susceptible to mechanical imperfections in the sensor. These imperfections may be due to misalignment of the sensor or the roughness of the reflector imparting noise on to the spectrum. Results from these imperfections can produce weaker peaks and valley for the

spectra than seen in Figure 1.8, making the determination of the maximum peak in the Fourier Transform more difficult.

1.3.3 Advantages and Disadvantages of Fiber Optic Sensors

The basic operating principles behind EFPI-based sensors yield distinct advantages over conventional electrical- and electromechanical-based sensors. Some advantages are directly related to the basis of the EFPI design and most commonly found within two operating regimes: environments with either high temperatures and/or high electromagnetic interference. These two types of environments are sometimes encountered during wind tunnel testing, which helps strengthen the idea that fiber optic sensors are attractive replacements for strain gage sensors on a sting balance.

Although these characteristics did not become a factor within this study, many instances of wind tunnel testing do encounter these problems. High temperatures are commonly found during combustion experiments or during hypersonic wind tunnel testing, where heat transfer effects are a common theme. High electromagnetic interference (EMI) can engulf wind tunnel experiments in some instances. In the Virginia Tech wind tunnels alone, EMI has played a major role in disrupting the output of some experiments such as during plasma torch testing or during experiments utilizing a traverse (due to the motor). Whatever the experiment, fiber optic sensors are essentially immune to electromagnetic interference (EMI) because the transducing technique used by the sensors does not involve electrical signals. Table 1.1 presents a direct comparison of foil strain gages and fiber optic sensors and reveals some other significant advantages.

Sensing Technology	*Advantages*	*Disadvantages*
Foil Strain Gages	• Low temperature sensitivity • Insensitive to pressure changes • Relatively low cost	• EMI sensitive
Fiber Optics	• Low temperature and EMI sensitivity • High sensitivity • Operability at extreme temperatures	• Higher cost • Possible pressure sensitive • Speed of current systems (66Hz)

Table 1.1 - Direct Comparison of Sensing Technologies

Another important aspect that should be discussed regarding this direct comparison is the resolution and accuracy. Although Section 2.1 – Choosing a Fiber Optic Sensor, explains the resolution and accuracy test in greater detail, a brief summary will be provided now to show the important advantage fiber optics have over conventional foil strain gages. A test specimen, as shown in Figure 1.9, was equipped with both fiber optic sensors and foil strain gages and then put through a loading cycle up to 35 Newtons. Results showed that the fiber optic sensor had a resolution of 0.002% full scale compared to the foil gages, which had a full-scale resolution of 0.01%. Also, the accuracy of the fiber optic sensor proved better than the foil gage, 0.8% and 1.0% full-scale, respectively. Table 1.2 is provided for direct comparison. Apart from the direct advantages of better resolution and accuracy, the increase in resolution allows the possibility of new balance designs with smaller sensors, thereby reducing the size of the balance. As previously mentioned, the size of the test section of a supersonic wind tunnel is inherently small. Therefore, a smaller balance could fit more easily into a smaller test model. Another advantage is that a smaller balance could increase the natural frequency response of the balance allowing it to be used in smaller models and tunnels.

	Foil Gage	**EFPI Embedment Sensor**
Resolution	0.01 % FS (0.1 με)	0.002% FS (0.02 με)
Accuracy	1.0% FS (10 με)	0.8% FS (8 με)

Table 1.2 - Resolution and Accuracy Comparison Between Sensors[7]

Another advantage seen in Table 1.1 is that fiber optics can be used in an operating range from –75ºC to 200ºC, yet with extremely low temperature sensitivity. This insensitivity to temperature is very important in supersonic wind tunnel testing in that the temperature may change markedly in the tunnel during operation.

A true visual size comparison between the sensors can best be seen in Figure 1.9, which shows the size difference between the embedded fiber optic sensor and the strain gage sensor on a wood test specimen. Figure 1.10 shows this relative difference on the front section of the AEDC sting balance. Please note that the fiber optic sensor has changed position from its location in this picture.

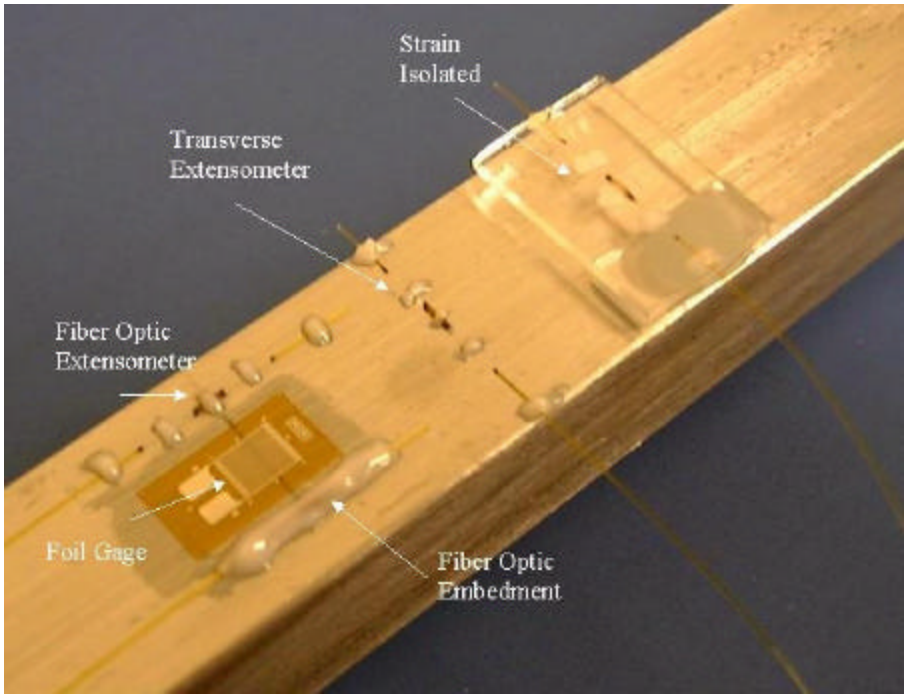

Figure 1.9 - Comparison of the Fiber Optic Embedment Sensor and a Foil Strain Gage

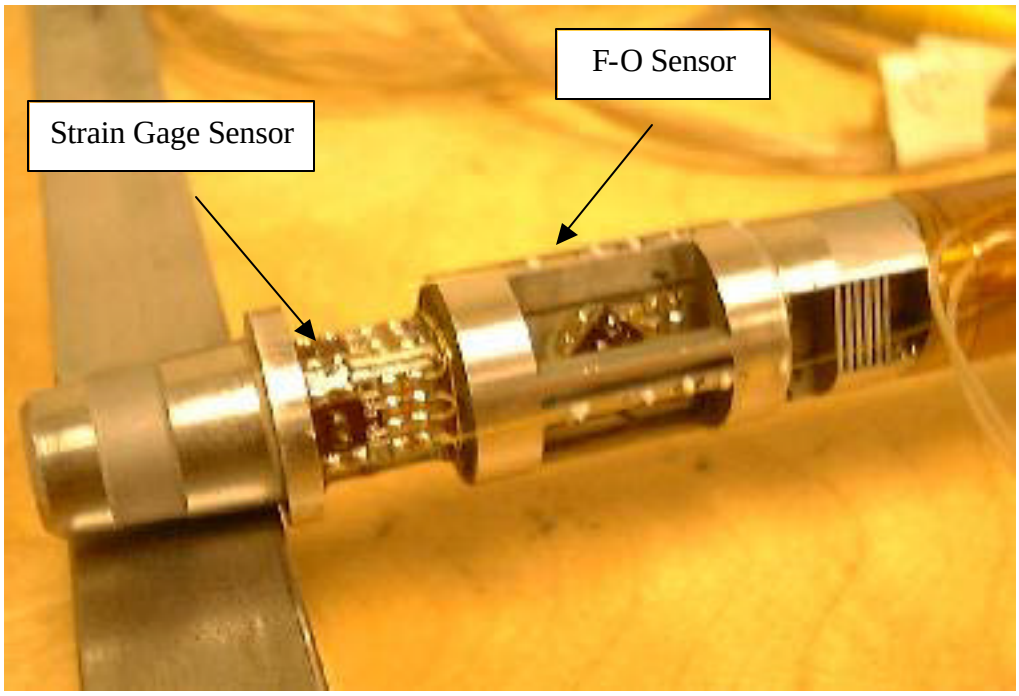

Figure 1.10 - Forward Section of AEDC Balance with Foil Strain Gage and Fiber Optic Sensor

Since the fiber optic sensors are so small, they are ideal for applications where restricted space or minimal measurement interference is a consideration, such as found on a sting balance. Another advantage is that the fiber optic sensor is somewhat easier to attach than the conventional strain gage sensor. Not only do strain gages require exact placement on the precisely machined balance, but they also require extremely delicate and time consuming wiring procedures to produce the Wheatstone bridge for temperature compensation. The time and money necessary for achieving these conditions all add to the overall cost of producing a highly accurate sting balance.

Placing fiber optic sensors on the sting balance nearly eliminates all these associated costs. First of all, the fiber optic sensors are less sensitive to their locations along the length of the balance as they have a better full-scale resolution and accuracy. Yet another possibility arises in that the fiber optics could be placed directly within the sting balance instead of on the exterior surface. Not only would this help protect the sensors from the harsh conditions associated with wind tunnel testing, but it could help decrease the effects which significant temperature changes could cause on the readings.

All of these facts lead to the conclusion that a smaller and more simply machined balance might be produced if fiber optic sensors were used in place of conventional strain gage sensors. This could lead to significant cost savings in both time and money. In regards to time, setup times would be significantly decreased because each sensor merely needs plugging in. Strain gages come equipped with many additional wires including excitation and sensing leads that must be connected to a signal-conditioning amplifier. In regards to cost, although the fiber optic sensors may cost more to produce than the conventional strain gages, the cost savings will be seen in the machining of the sting balance.

Chapter 2 – Fiber Optic Sting Balance

The development of this trial application of new fiber optic sensors on a sting balance required many important considerations prior to the installation of the fiber optic sensors. It was first decided that the sensors would be placed on the AEDC balance in conjunction with the strain gage sensors, so that real time comparisons could be made between the data collected by the conventional foil strain gages and the fiber optic sensors. After this decision was made, it was necessary to determine where to place the sensors on the AEDC balance and what type of fiber optic sensors were to be used for the experiment.

2.1 Choosing A Fiber Optic Sensor

Luna Innovations researchers considered two types of sensors for placement on the AEDC sting balance. Development of both the embedment and extensometer EFPI strain sensor designs continued in order to increase the resolution and accuracy of the sensors. Although both designs consist of two optical fibers positioned within a hollow-core silica tube, the differences exist in the securing of the fibers in the tube and in attaching the sensor to the sting balance, as can be seen in the right hand side of Figure 1.7. In the embedment sensor, both fibers are secured to the tube with an epoxy. The epoxy is then used to secure the sensor to the specimen by fully encapsulating the sensor and attachment area. In the extensometer design, the fibers are not fixed to the hollow-core tube, removing the induced strain from the sensor itself and thereby improving the fatigue performance. Epoxy is again used to attach the sensor, but in three separate locations, instead of encapsulating the entire sensor.

Luna Innovations researchers instrumented a test specimen, as seen in Figure 1.9, with two foil sensors (Foil 1 and Foil 2), a fiber optic extensometer (FO Ext), and an embedded fiber optic sensor (FO Emb). The specimen was then run through a loading cycle from 0 to 35 kN, and back to 0. Results from this are presented in Figure 2.1,

which shows that the embedded sensor provides more accurate results than both the extensometer and the two foil gages. These numbers were determined by taking the measured noise (about 0.1 microstrain) and dividing that by the known yield loading of the test specimen, thereby representing the error in percent full scale load (% FS).

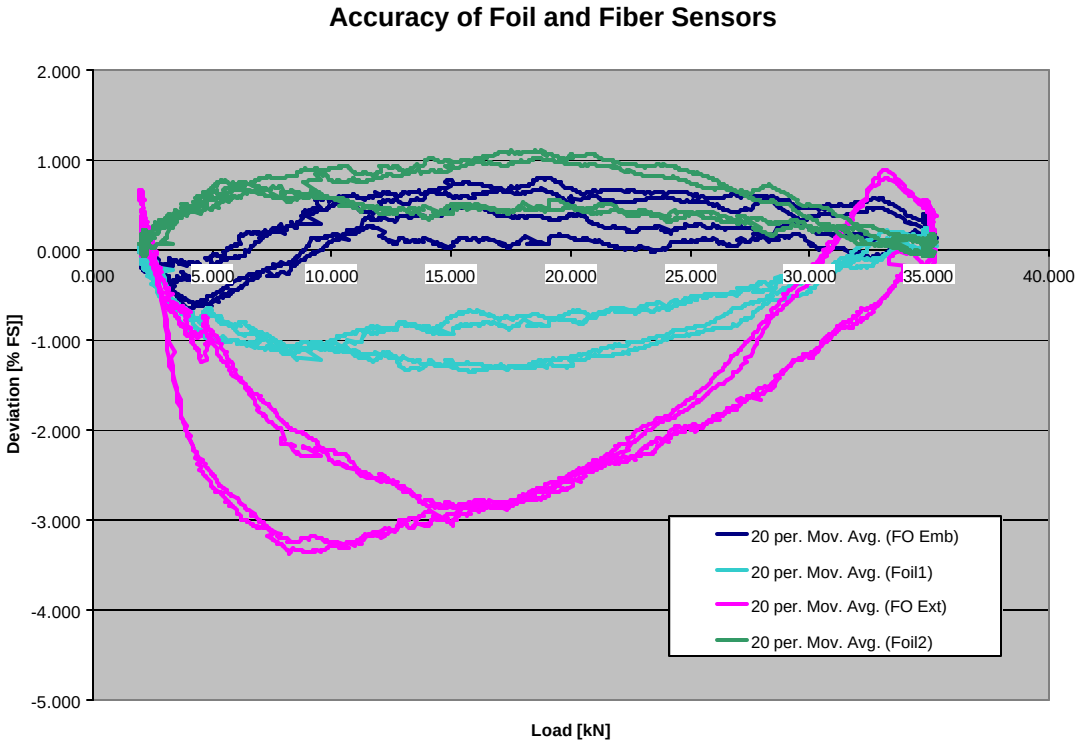

Figure 2.1 – Accuracy Comparison of Different Fiber Optic Sensors and Foil Strain Gages on Load Specimen[7]

In order to determine the resolution of the embedment sensor, the response over time for a 35 kN load cycle is provided in Figure 2.2. The dynamic range for the sensor is 14 microns for full-scale movement as shown in the plot. To show the steady-state performance of the embedment sensor, a plot of the first 50 seconds of the data is shown in Figure 2.3. It can be seen that the stability of the sensor output is better than 0.2 nm (0.0002 microns). This results in a sensor resolution of 14 over 0.0002 microns, or better than 0.002%.

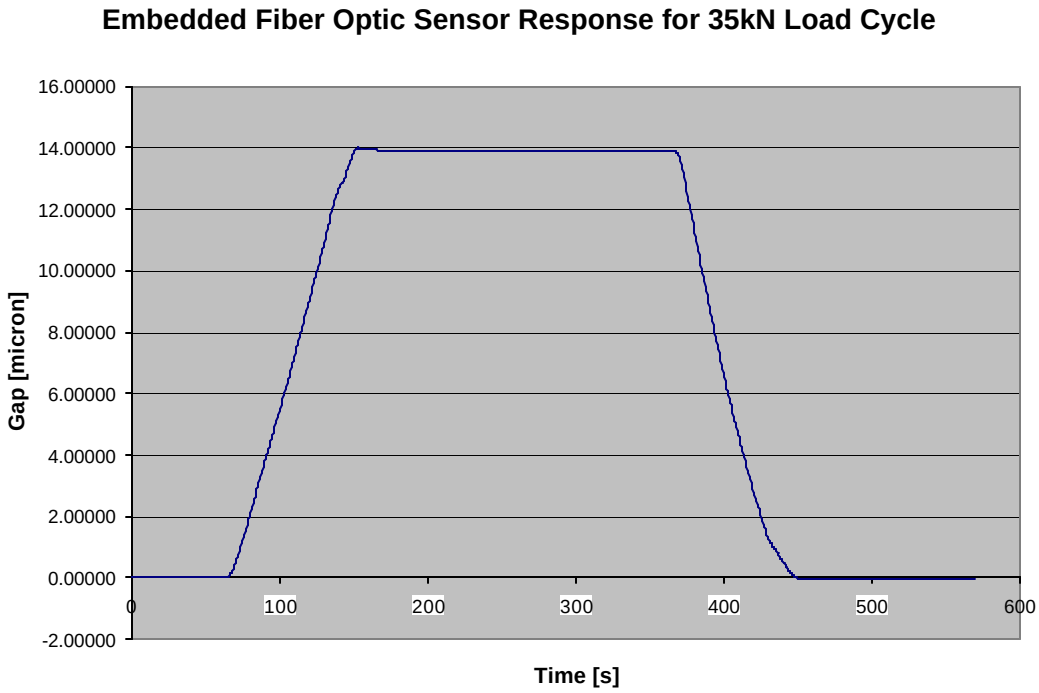

Figure 2.2 – Fiber Optic Embedment Sensor Response for 35 kN Load Cycle[7]

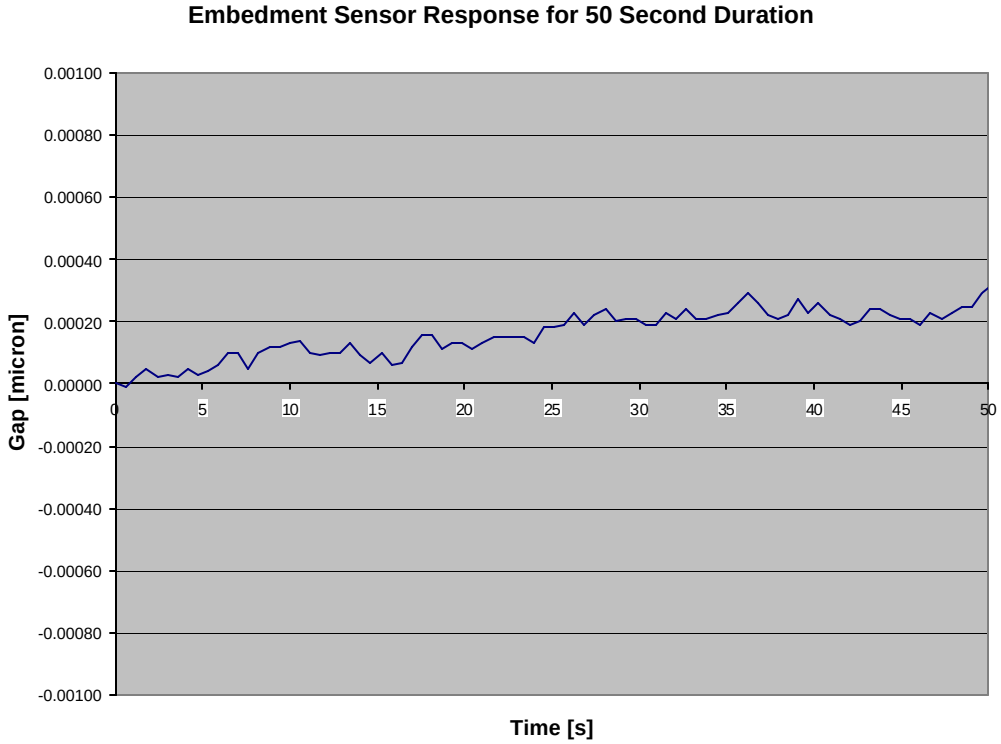

Figure 2.3 - Response During First 50 Second Duration of 35 kN Load Cycle[7]

Table 2.1 reviews the performance characteristics of the EFPI embedment strain sensor as compared to foil strain gages found during the load cycle testing study.

	Foil Gage	EFPI Embedment Sensor
Resolution	0.01 % FS (0.1 με)	0.002% FS (0.02 με)
Accuracy	1.0% FS (10 με)	0.8% FS (8 με)

Table 2.1 – Resolution and Accuracy Comparison[7]

2.2 Sensor Location

One concern regarding the placement of the fiber optic sensors is the constraint on running the fiber optic leads. The leads need to run safely from the sensor locations along the length of the balance and then down and out of the wind tunnel to the *Fiberscan* unit. This process must be completed without damaging the balance. Another major consideration for placing fiber optic sensors on the pre-existing sting balance is determining the locations on the balance that will receive nearly the same order of magnitude of strain as the locations of the foil strain gages. Obviously, the fiber optic sensors cannot be placed directly over the strain gage sensors for fear of damaging or changing the physical properties of the strain gages. Therefore, a finite element analysis (FEA) was performed on the AEDC sting balance to help determine locations for the placement of the fiber optic sensors. Dr. Rakesh Kapania and his student Yong Yook Kim helped complete this area of the study.

A solid 3-D finite element model representing the geometry of the 6-component AEDC balance was developed using PATRAN/NASTRAN software. First, a model closely representing the detailed geometry of the balance was developed via MSC/PATRAN as seen in the isometric solid model rendering of Figure 2.4. Next, the specific material properties of the balance were put into the coding. These properties were found by

researching the type of steel detailed in the engineering drawings provided with the balance. The material is stainless steel 17/4 with the following properties:

Modulus of Elasticity, E:	197 Gpa
Poisson's Ratio, ν:	0.272
Material Density, ρ:	7.81 g/cm^3

Finally, a tetrahedral element meshing method was chosen because of its ability for meshing solids with complex shapes. The constructed solid model using tetrahedral elements could have been developed with a finer mesh if a higher resolution had become necessary. Results of this meshing method can be seen in Figure 2.5.

Figure 2.4 - Solid Model CAD Rendering of AEDC Balance

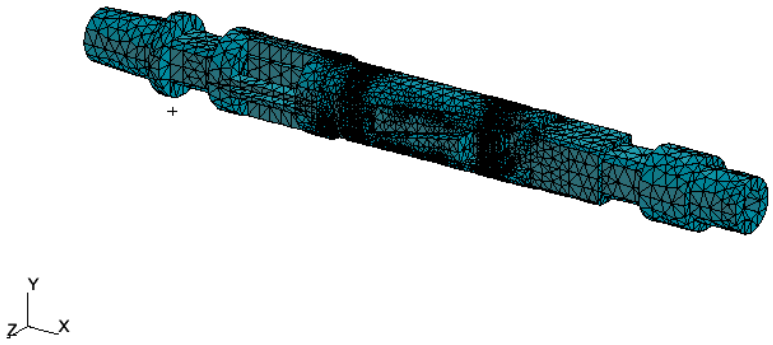

Figure 2.5 - Finite Element Model (FEM) with Tetrahedral Meshing Configuration

Development of this Finite Element Model (FEM) allowed the stress, strain and displacement of any region of the AEDC balance to be determined for various loading cases. Precise numerical results could be obtained at any location where a nodal point was positioned. A load case was performed with the virtual application of a 12.36-pound (55 Newton) force on the tip of the balance. Figure 2.6 shows the expected stress of the balance in the x-direction with the color-coding representing stress in psi.

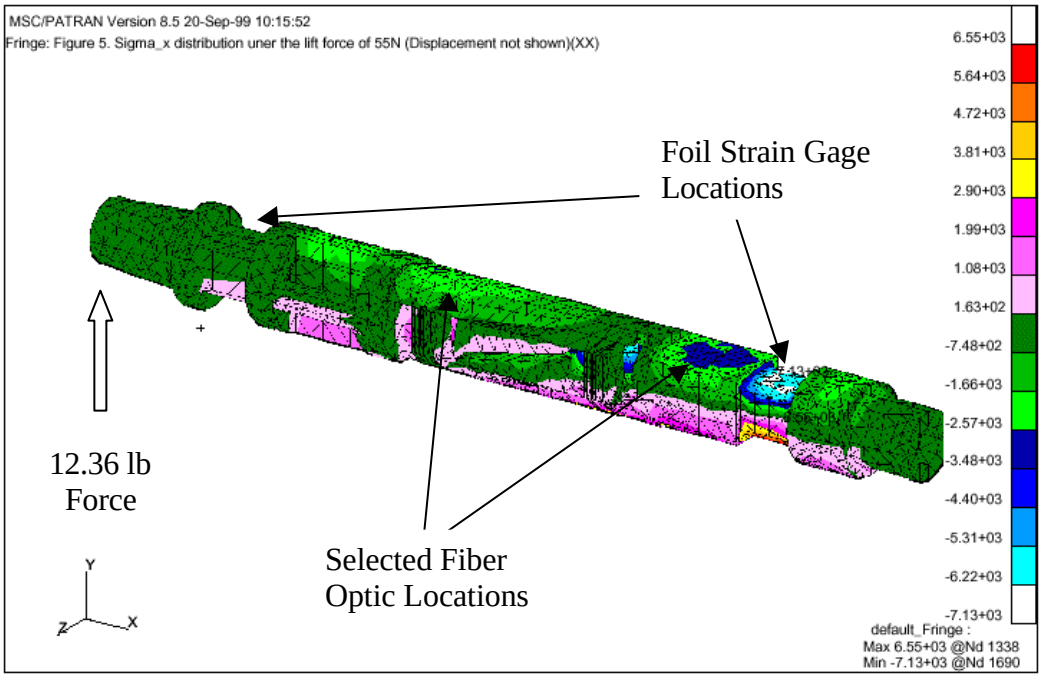

Figure 2.6 - Fiber Optic Sensor Locations

The locations determined for placement of the fiber optic sensors can also be seen in Figure 2.6. From this model, we can deduce that the forward and aft foil strain gages will experience approximately 750 PSI and 7000 PSI, respectively. While the chosen fiber optic locations will provide approximately 2500 PSI in the forward section and 3500 PSI in the aft section of the balance.

One important aspect to be considered when using the finite element model is the validity of the results obtained through the PATRAN/NASTRAN software. In order to validate the results, it was necessary to compare the stress encountered by the strain gages and the

stress obtained through the modeling program. The stress determined by the strain gage sensors was calculated by first finding K, the gage factor. Equation 2.1shows the gage factor for a full Wheatstone bridge in terms of a voltage output (V_{out}), a constant voltage input (V_{in}), the modulus of elasticity (E), and the stress (σ_{xx}).

$$K = (V_{out}/V_{in})*(E/\sigma_{xx}) \quad (2.1)$$

The engineering drawings provided with the balance contained all the pertinent information for determining the gage factor and resulted in a gage factor of 2.00. Equation 2.1 was then rearranged to solve for the stress, σ_{xx}, at the forward and aft strain gage sensor locations. A constant input voltage of 5.0 volts was used in the setup of the experiment with the calculated gage factor of 2.00 and modulus of elasticity of 28,572,880 psi. Output voltage was then taken directly from the strain gage sensors during the test run in order to determine the stress at both the forward and aft strain gage locations. Since the FEM was developed for a 12.36 lb normal force applied at the tip of the balance, a linear extrapolation was performed on the experimental results since those results determined a normal force of only 7.69 lbs. Application of Equation 2.1 and the linear extrapolation resulted in the calculations provided in Table 2.2. The results show that the FEM corresponds well to the actual stress encountered by the strain gage sensors. Results show the error in the FEM was better than 6% in the forward and aft balance locations.

σxx	***Experimental Results***	***FEM Results***	***Error***
Front Location	-710 psi	-748 psi	5.4 %
Aft Location	-6,944 psi	-7,130 psi	2.7%

Table 2.2 – Comparison of FEM and Experimental Stress Results

2.3 Calibration of the Fiber Optic Sting Balance

Access to the proper equipment for a precise calibration was limited. Therefore, only the primary sensitivity terms were determined on-site at the Virginia Tech campus. This leads to a large assumption that there are no interactions between the fiber optic sensors as mentioned in the strain gage calibration section. This assumption is acceptable here due to the nature of the wind tunnel setup for this study. The blunt cone model will be placed at an angle of attack in order to induce a pitching moment and normal force. As the model will be centered along the tunnel section, no yawing moment or side force should affect the model. Therefore, fiber optic sensors were not be placed on the sides of the balance to measure the side force and moment. Only direct pitching moment data will be taken from the balance and the possible side force interactions were thus neglected. If a small side force or yawing moment does actually affect the sting balance, this will produce a relatively small error in the results for both the foil strain gages and the fiber optic sensors.

Originally, four EFPI-based sensors were placed on the sting balance and calibrated. They were placed on the top and bottom of both the forward and aft locations shown on Figure 2.6. After further analysis, it was determined that the top front sensor, T1, and the bottom aft sensor, B2, provided the most accurate and repeatable results. Fiber optic sensor T2 was broken during the calibration procedure, and B1 appeared to be calibrated incorrectly or may have also been damaged after the calibration procedure. When B1 was recalibrated after wind tunnel testing, it produced approximately four times the expected output, as will be shown in the Results section. Therefore, only the calibration of the two sensors T1 and B2 will be presented. A calibration bar was developed to allow the application of known weights at half-inch intervals from the tip of the balance, as shown in Figure 2.7. The calibration procedure consisted of placing known weights at these locations, thereby causing a change in the pitching moment.

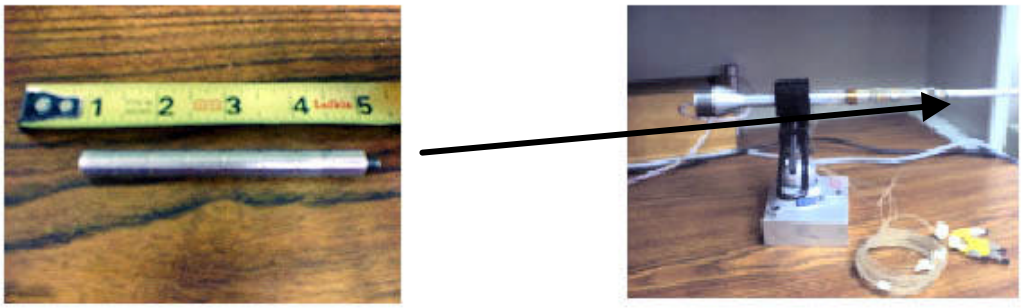

Figure 2.7 - Calibration Bar on AEDC Sting Balance

Since the exact distance of the fiber optic sensors from each weight loading is known, it is possible to plot the actual pitching moment (in-lbs) versus the change in voltage. Although it was explained earlier that the fiber optic sensor actually determines a change in gap distance, this gap distance can be changed to a voltage using a *Fiberscan* unit, a commercially available product designed and developed by Luna Innovations, Inc. The *Fiberscan* system allows the user to amplify and convert the distance read by the fiber optic sensor into a voltage signal. Plots revealing the linear response of sensors T1 and B2 can be seen in Figure 2.8 and Figure 2.9. A linear regression was then performed on the calibration data to obtain the slope, the inverse of the primary sensitivity. After determining the primary sensitivity for each sensor, one can then multiply all output from the wind tunnel tests by this number to determine the pitching moment at each sensor location.

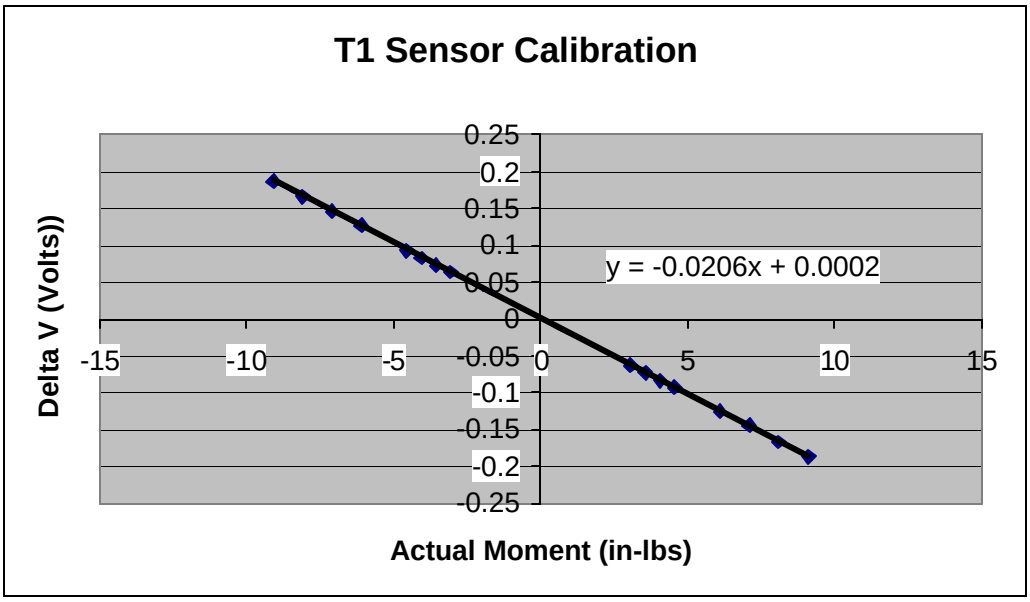

Figure 2.8 - Sensor T1 Calibration and Linear Regression

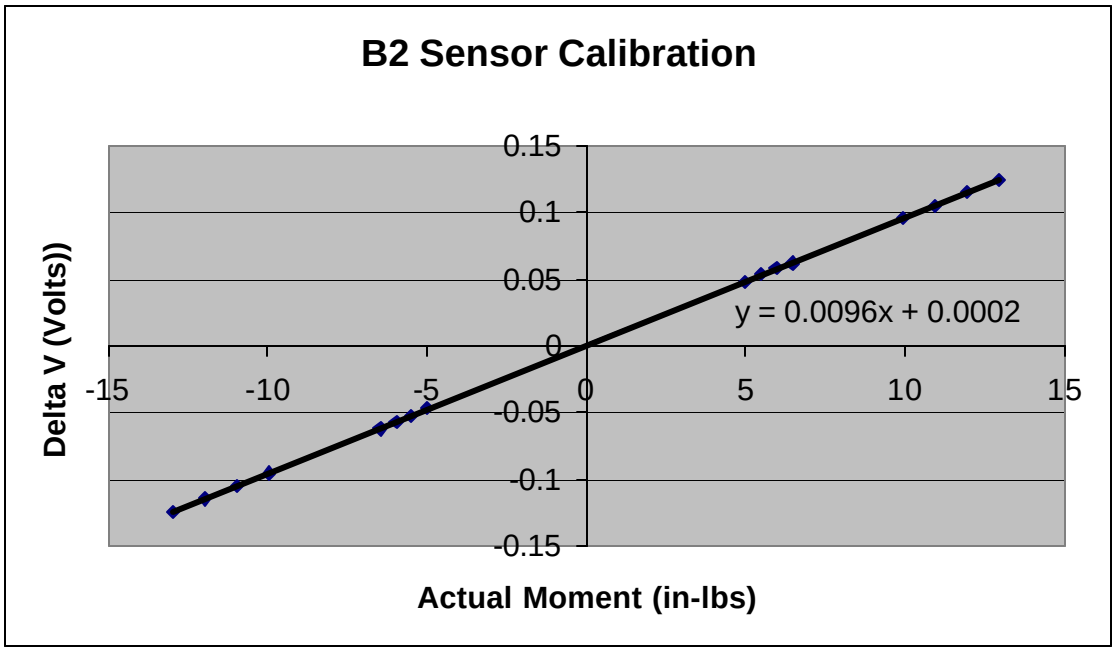

Figure 2.9 - Sensor B2 Calibration and Linear Regression

Chapter 3 – Experimental Setup

To ensure precise and repeatable measurements from the balance, care was taken in the design and implementation of all associated equipment for this study. In this chapter, a detailed description of the experimental setup used for testing the fiber optic sting balance is provided, including information on the facilities, equipment and model used.

3.1 Facilities and Equipment

The campus of Virginia Tech contains several high-quality wind tunnels, which were obtained directly from NASA. The research for this study was conducted in the Virginia Tech 23x23 cm supersonic/transonic wind tunnel that was purchased in 1958 by Virginia Tech from NASA Langley Research Center, where it was originally designed and constructed. The compressor can pump the storage system up to 51 atmospheres and the settling chamber contains a perforated transition cone, several damping screens, and probes which measure stagnation temperature and pressure. There are three complete nozzle chambers that are currently fitted with nozzle contours for Mach numbers 2.4, 3.0, and 4.0. Shadowgraph pictures of the flow were taken with a focused shadowgraph arrangement utilizing a parabolic mirror and a 1-microsecond spark source. Data acquisition for all measurements is IBM PC based using modern software such as LabView. Test conditions for the experiments are presented in Table 3.1.

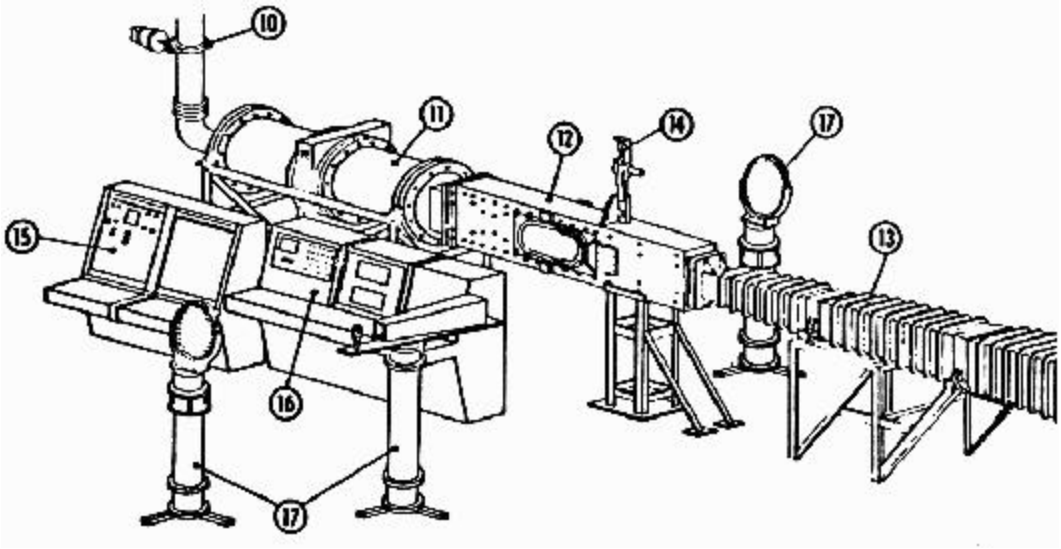

Figure 3.1- Supersonic Wind Tunnel Layout

10-Pressure Regulator, 11-Settling Chamber, 12-Test Section, 13-Diffuser,
14-Model Support and Drive System, 15-Tunnel Control Panel,
16-Measurement Panel, 17-Schlieren Apparatus

In order to securely hold the sting balance and model during operation of the wind tunnel, it was necessary to design a strong and durable tunnel model mount plate. The tunnel plate is a half inch thick piece of aluminum, which is designed to fit tightly into the floor of the test section. Protruding upwards from this tunnel plate is the arm that holds the sting balance. Before this arm could be developed, prior analysis was essential for two major reasons:

1) If the arm were not designed aerodynamically, unwanted shockwaves could be produced, which could influence and interact with the airflow and severely damage the sting balance.
2) If the arm were too large, blockage within the wind tunnel test section could occur, resulting in extremely turbulent subsonic flow.

Another component in the design of the tunnel plate was the requirement of an adjustable angle of attack (AOA). This was incorporated using an adjustable pin design below the

tunnel plate and allowed for sting placement at 0, 2 and 10 degrees AOA. Figure 3.2 shows an isometric solid CAD rendering of the tunnel plate design along with a side view to show the design of the undercarriage. The fiber optic leads that run from each sensor along the length of the balance track down through a front hollowed-out section of the arm, as shown in Figure 3.2.

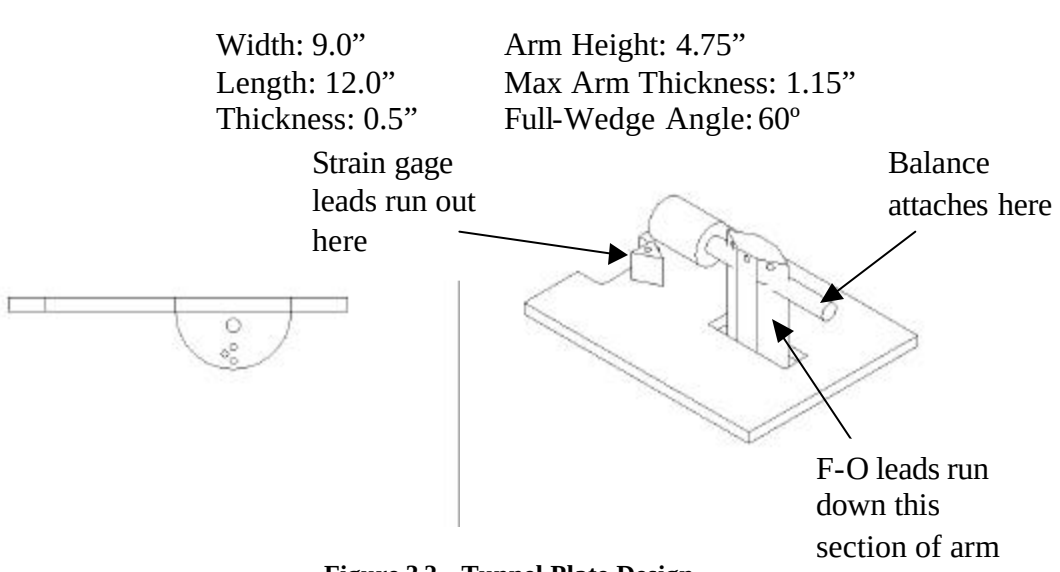

Figure 3.2 - Tunnel Plate Design

With the busy and highly regulated supersonic wind tunnel schedule, it was necessary to design the tunnel plate for fast and easy setup. Therefore, it was developed so that calibration procedures for the sting balance could be accomplished outside of the tunnel. When finished with the calibration, the plate could simply be set into place in the tunnel, and it would be ready for testing. Figure 3.3 shows the tunnel plate and sting balance placed inside the test section with the calibration bar still attached.

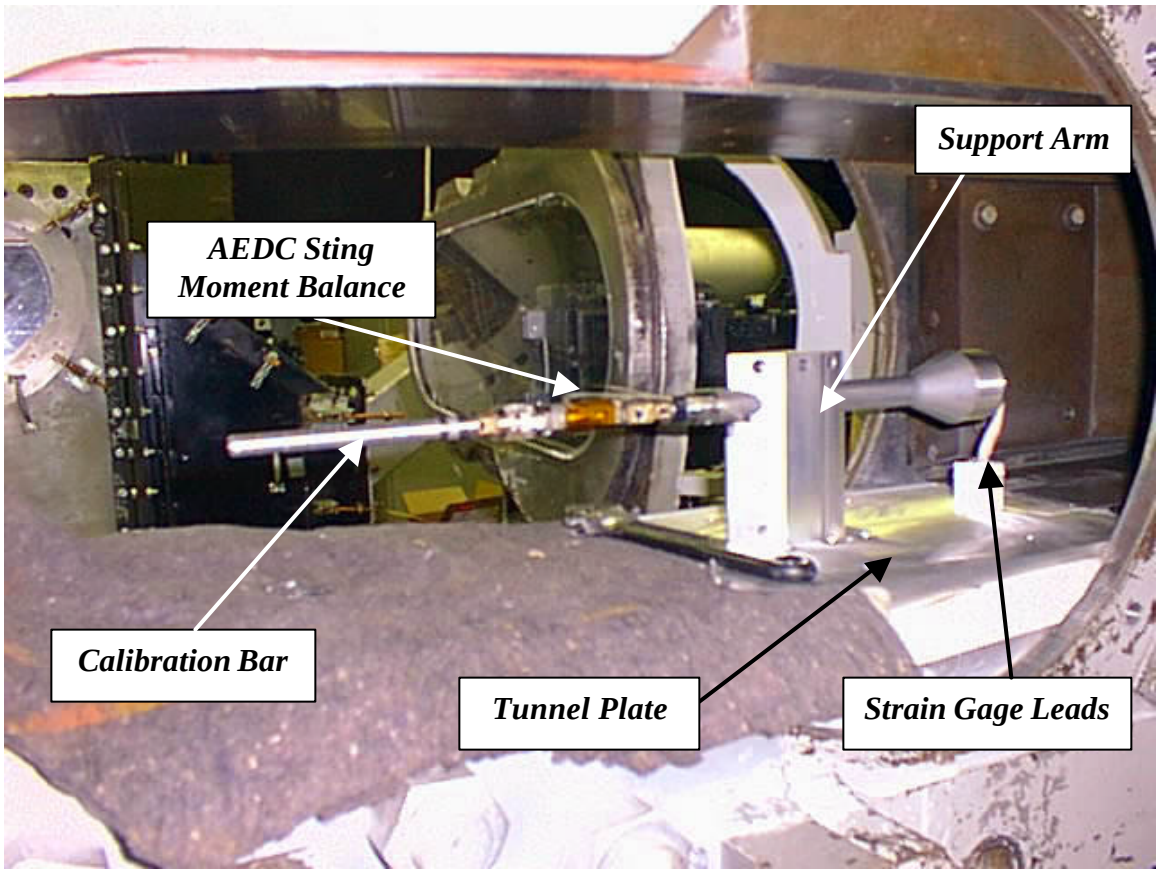

Figure 3.3 - Placement of Sting Balance in Wind Tunnel Test Section Immediately Following Calibration Procedure. The Cone Model Is Not Present Here.

3.2 Test Model

Another step in preparing for the study was to find or create a suitable model that would provide sufficient forces and moments that could be determined by both sensor systems on the balance. The model also had to allow for these forces and moments to be relatively easy to predict in order to verify the experimental results. The model that was designed and built for use in the Virginia Tech Supersonic Wind Tunnel was a 10º blunt cone, resembling the front nose of a missile. The model has a base diameter of 3.0 inches and a blunt nose with a radius of 0.25 inches. It was machined of aluminum. The blunt nose of the cone was designed to be detachable so that a sharp nose could also be placed on the model. This additional design was added for correction purposes in the case that

blockage effects were found present in the tunnel test section. Analysis of the setup prior to testing confirmed that blockage effects were of minimal concern, but to ensure this, the base area of the model was reduced by 20% to reach the current base diameter of 3.0 inches. The analysis was accomplished by calculating the maximum permissible model frontal area for closed test sections as a function of Mach number and drag coefficient. Figure 3.4 shows the cone model on the sting balance inside the wind tunnel test section.

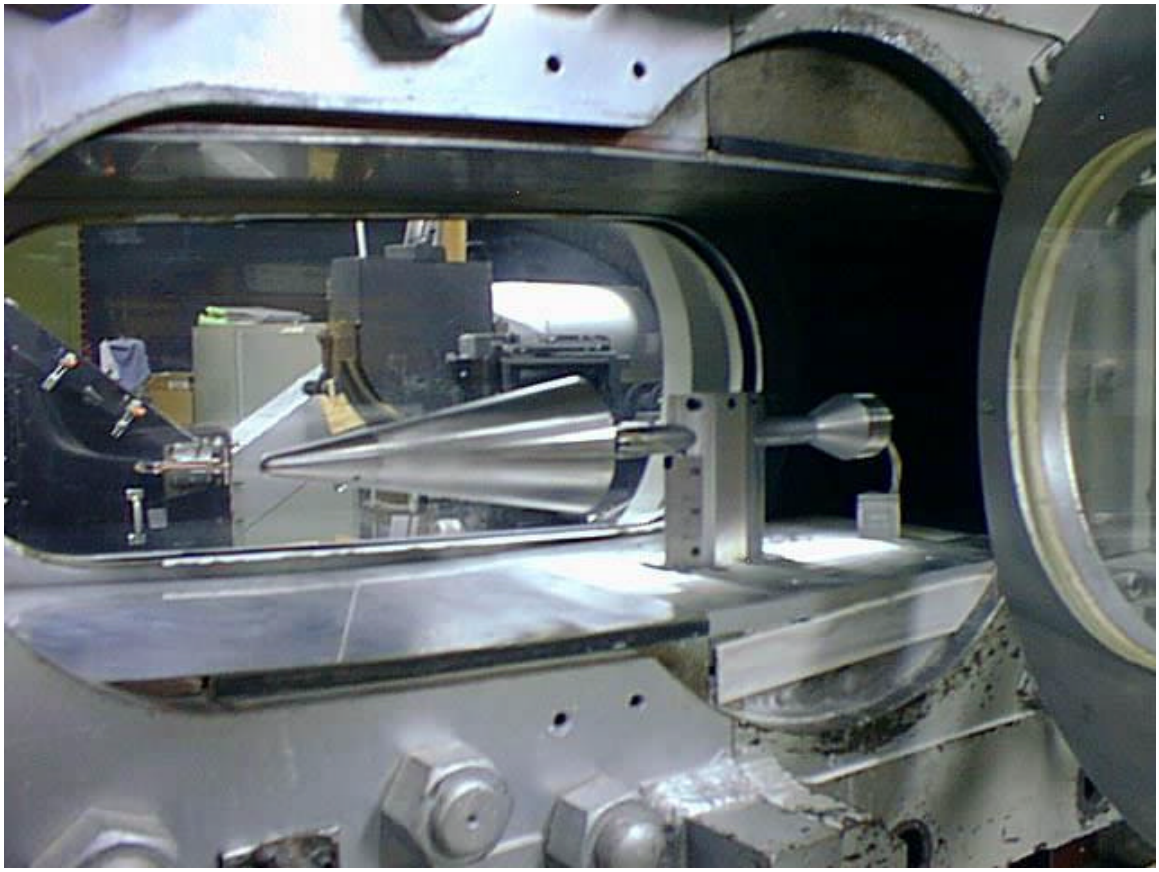

Figure 3.4 – Blunt Cone Model Inside Tunnel Test Section

Dr. Joseph Schetz and his graduate assistant Valerio Viti helped make predictions of the forces and moments on this model using computational fluid dynamics (CFD). The CFD software used was GASP, a finite volume code developed and owned by AeroSoft, Incorporated. Inviscid calculations of the cone were produced at Mach 2.4 at a nominal AOA of 2.3º. This nominal AOA was determined from shadowgraphs and will be explained in greater detail later. A picture of the model cone and the flow field grid as

seen in the GASP program is shown in Figure 3.5. A base pressure correction factor was not included in the CFD predictions because the base is essentially parallel to the y-direction (as shown in Figure 3.6) and therefore it does not affect the normal force. Since there is an equal amount of area above and below the x-axis, the pitching moment would also not be affected.

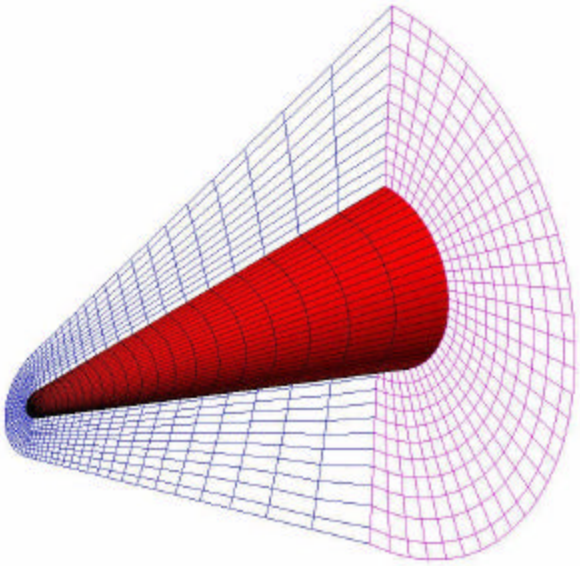

Figure 3.5 - Representation of the Cone in GASP

The CFD predictions were run corresponding to the conditions experienced during testing. The atmospheric conditions and the calculated results from GASP are presented in Table 3.1. The flow field representation generated by GASP at these conditions is provided in Figure 3.6.

Atmospheric Conditions		***Calculated Results***	
Mach Number	2.4	***Mach Number***	2.4
Nominal AOA	2.3°	***Nominal AOA***	2.3°
Stag. Pressure	55 PSIA	***Pitching Moment***	13.5 in-lbs
Stag. Temp.	77.5 °F	***Normal Force***	8.2 lbs

Table 3.1 – CFD Conditions and Results

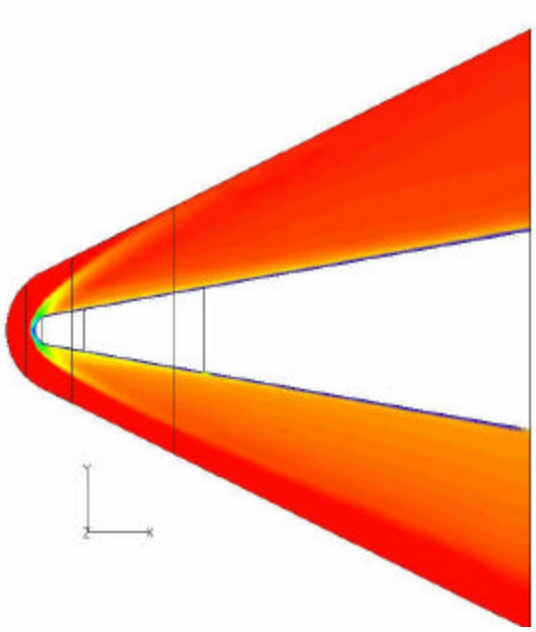

Figure 3.6 - Mach Number Contour Lines for the Inviscid CFD Predictions

Chapter 4 – Experimental Results

Results were obtained from the Supersonic Wind Tunnel by way of the foil strain gage sensors and the embedded fiber optic sensors. Shadowgraph flow visualization techniques were also used in order to verify any flow field interactions that may affect the output of the sensors and also as a rough redundant check to prove that Mach 2.4 was attained using shock angle relations.

4.1 Initial Results

The experimental process began with a dummy balance that was created by the Virginia Tech AOE shop staff. The dummy balance was used in order to find the optimal conditions for running the model at Mach 2.4. These recorded conditions included initial tank pressure, input pressure, steady state stagnation pressure in the tunnel, and the pressure control valve settings, which can be seen in Table 4.1. The tunnel settings and optimal conditions often need to be refined slightly depending on the model being tested and the associated run time. Testing with the dummy balance proved to be a highly valuable process. Many tunnel settings were found where the tunnel would simply not start, causing the model to vibrate wildly. This sort of oscillation could have easily damaged the balance, but this was fortunately avoided during testing of the real balance.

Mach Number	Angle of Attack(AOA)	Tank Pressure	Input Pressure	Stagnation Pressure (SS)	Hydraulic Valve Setting
2.4	2.3°	300 PSI	77 PSI	55 PSIA	9.74 Volts

Table 4.1 - Tunnel Settings and Conditions

It was also necessary to visualize the flow around the model and balance at Mach 2.4 for a few reasons. First, it was necessary to prove that the model was actually reaching Mach 2.4, as this speed was being used for the CFD predictions. Secondly, we had to make

sure that shock waves were not interacting or reflecting in such a way that would damage the balance or confuse the interpretation of the results. Therefore, shadowgraphs were taken of the flow field at the nose of the cone model and at the base of the cone, which includes the arm holding the sting balance. The shadowgraphs are shown in Figure 4.1 and Figure 4.2. The flow is from right to left. A horizontal reference line was included in Figure 4.1, the shadowgraph of the model nose, to help determine the actual AOA of the cone model after start-up of the tunnel. The model was set at a nominal 2° AOA prior to tunnel startup, which after reviewing the shadowgraphs yielded an actual AOA of 2.3° during tunnel operation. The determination of the nominal AOA was accomplished by comparing two shadowgraphs. The first shadowgraph was taken without operating the tunnel, whereas the second shadowgraph was taken during a test run. After comparing each shadowgraph to the horizontal reference line, it was found that the AOA changed from 2º to 2.3º during tunnel operation. Figure 4.2 shows the lower half of the shockwave reflecting off the bottom of the test section. Although a shockwave is also produced in front of the arm, there are no unwanted interactions with the model base flow or sting balance.

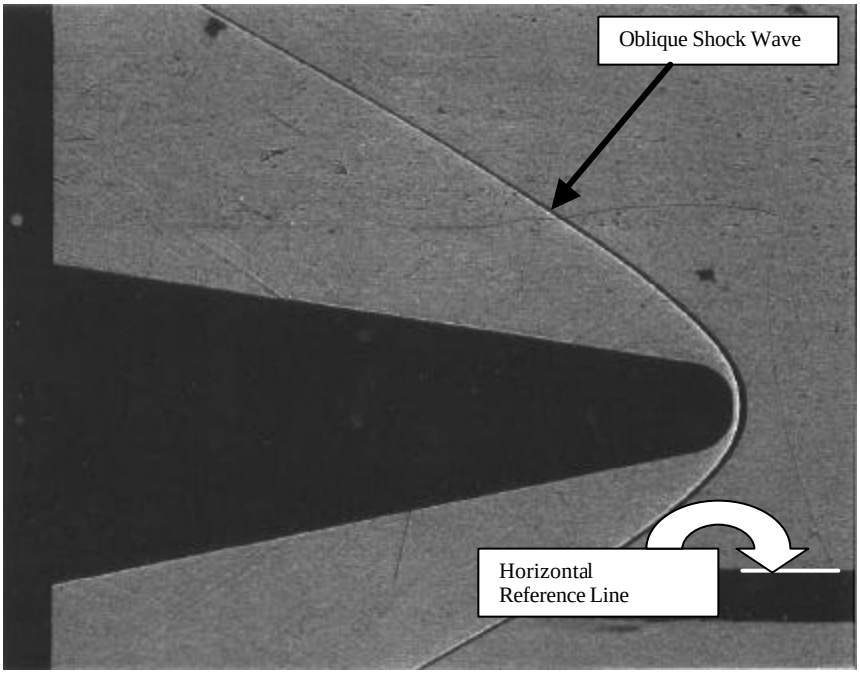

Figure 4.1 - Front Shadowgraph (2.3º AOA)

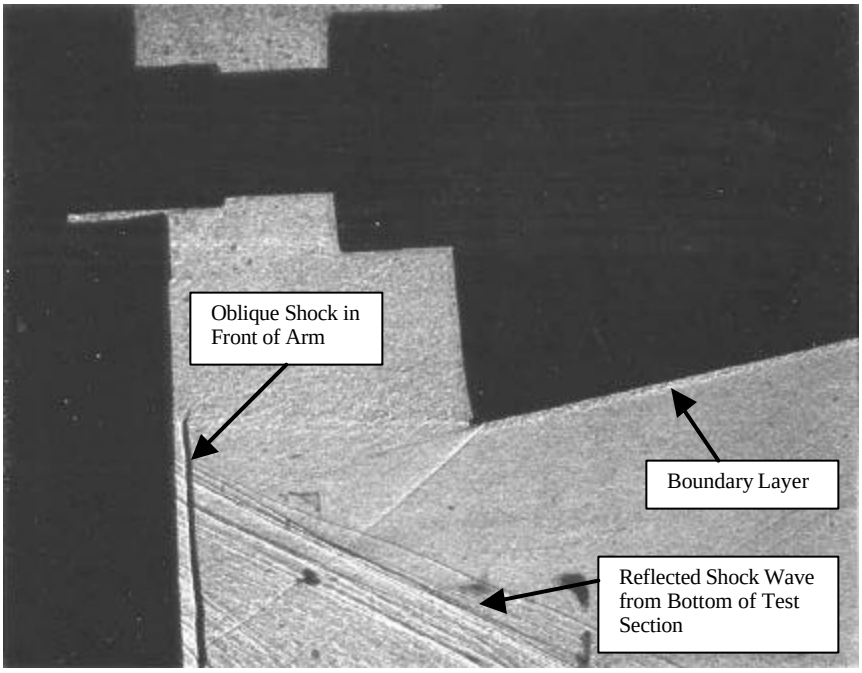

Figure 4.2 - Back Shadowgraph (2.3º AOA)

4.2 Foil Strain Gage and Fiber Optic Sensor Results

After finding the optimal tunnel settings and run conditions, the real balance, equipped with both strain gage and fiber optic sensors, was placed inside the tunnel test section at a nominal 2° AOA. The strain gage sensors were connected in order to measure the pitching moment, normal force and axial force. Although only pitching moment and normal force readings were compared to the fiber optic readings, axial force was added in order to protect the AEDC sting balance. Testing of the balance prior to the addition of the fiber optic sensors showed that the balance was reaching its design load limits during start-up of the blow down tunnel. Unfortunately, in wind tunnels whose dynamic pressures are high, the increase in loading during the starting and stopping of the airflow can be large. The starting phenomena are random and therefore nearly impossible to predict without sufficient measurements to assure a statistically reliable answer.[17] Although the force and moment measurements came close to the design load limits

during startup of the blow-down tunnel, the forces and moments leveled out to acceptable readings once the tunnel reached supersonic speeds.

Raw data was taken from both the foil and fiber optic sensors using the Labview software program and saved on a computer hard drive. After processing each set of data with their corresponding calibration matrix, moments were determined at all sensor locations. When analyzing the results from the experiment, it was assumed that the foil strain gage results were providing accurate results. This allows one to use the pitching moment and normal force foil strain gage results to reference the pitching moment to any location along the sting balance. This is accomplished using Equation 4.1 where M_o is the measured pitching moment at the strain gage pitching moment location, N is the measured normal force, and x_{ref} is the distance from the strain gage pitching moment location to the desired reference point. In this case, the desired reference point is the location of the front fiber optic sensors.

$$M_{ref} = M_o + N*x_{ref} \tag{4.1}$$

Therefore, the strain gage pitching moment readings were referenced to the forward fiber optic pitching moment location. Results have been plotted in Figure 4.3 using a Microsoft Excel-based 15% moving average to show a comparison of the strain gage pitching moment and the two front fiber optic pitching moment results. The y-axis on the left shows the pitching moment (in-lbs) versus time (seconds), while the y-axis on the right shows the total stagnation pressure (psi) in the supersonic wind tunnel during the test run. When the tunnel first starts, a large force is briefly applied to the model and balance, which is due to the additional loads incurred during the starting of the airflow. Fortunately, once supersonic speeds were reached, the force decreased to a smaller, more constant loading level.

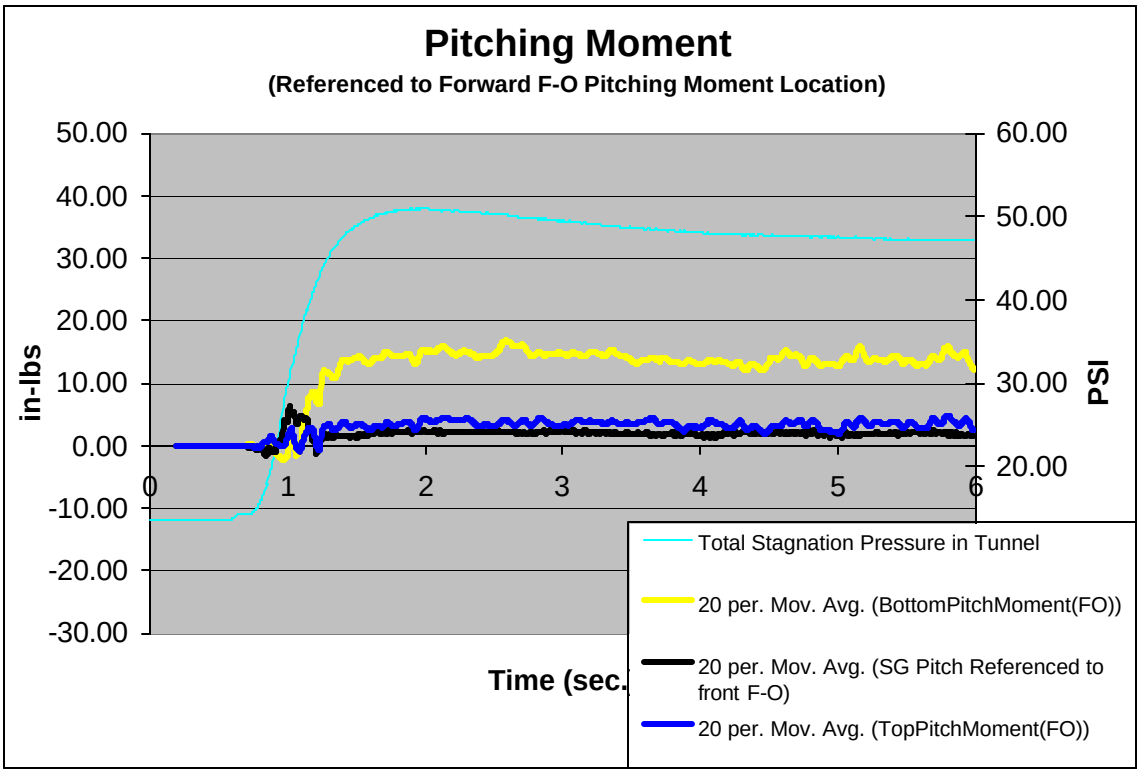

Figure 4.3 - Pitching Moment Calculations Referenced to Forward F-O Sensor Location

This figure reinforces the point made in the fiber optic calibration section, which stated that fiber optic sensor B1 (front bottom sensor) was not working properly. After recalibrating all the sensors, it was found that sensor B1 was now giving nearly four times the expected output. This is verified in Figure 4.3, which shows the readings from sensor B1 at approximately 16 in-lbs, whereas the actual readings are only around 4 in-lbs. This change in sensor output may have been caused by loose or weakened epoxy inside the embedment fiber optic sensor that could have resulted from a vibration within the sensor from the startup load. We also see from Figure 4.3 that fiber optic sensor T1 (front top sensor) corresponds well to the pitching moment measurements made by the strain gages.

It is now necessary to show that the bottom back fiber optic sensor (B2) is working properly by referencing the strain gage pitching moment to the back fiber optic sensor location. The strain gage measurements are referenced to each of the fiber optic locations

in order to check that the fiber optic sensors are working properly and can be used to determine the normal force. Since sensor T2 was broken during the calibration procedure, proof showing that the other back fiber optic sensor B2 is provided in Figure 4.4. The pitching moment of the foil strain gages and the fiber optic sensors at the back fiber optic sensor location versus run time is shown in Figure 4.4 using a 20% moving average. This figure shows that the strain gage measurements are comparable at the back fiber optic pitching moment location. In Figure 4.4, the total ambient pressure finally steadies out at about 47 PSI and the pitching moment at the back fiber optic locations is about 17 in-lbs for both the foil strain gages and the fiber optic sensors.

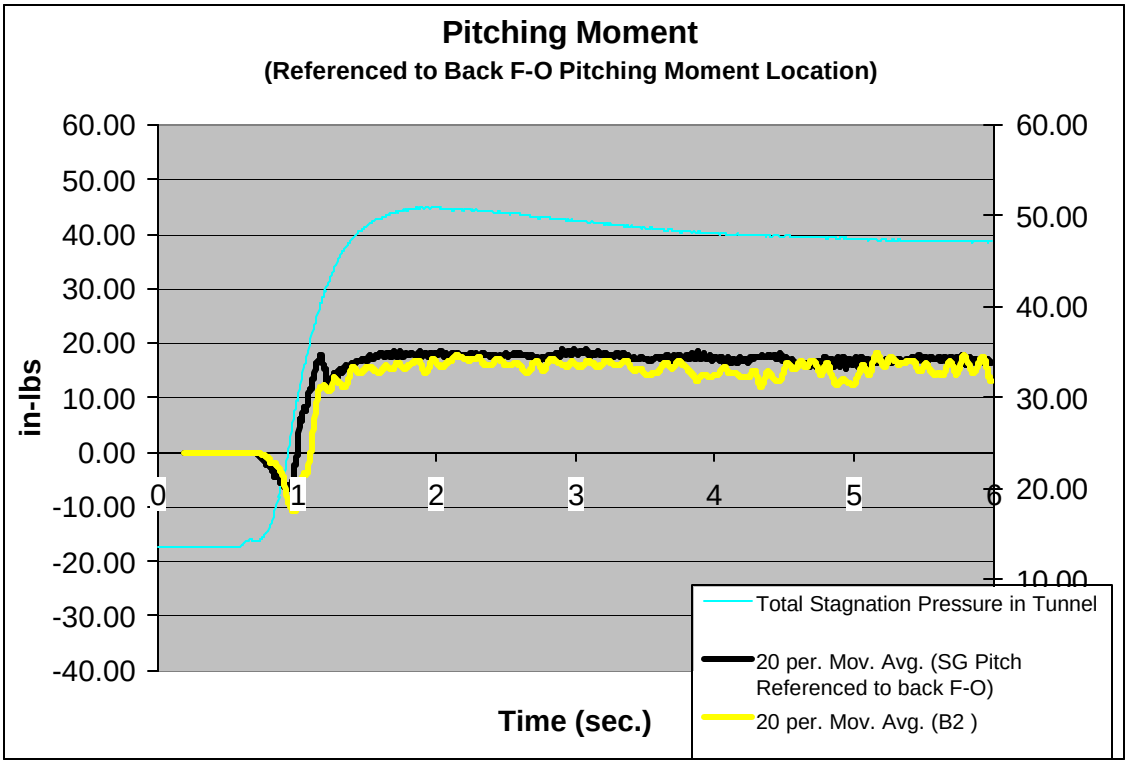

Figure 4.4 - Pitching Moment Calculations Referenced to Back F-O Sensor Location

Results from Figures 4.3 and 4.4 show that measurements from fiber optic sensors T1 and B2 correspond to the strain gage readings at the desired reference locations. Therefore, the normal force can now be determined using these measurements from sensors T1 and B2. With Equation 1.1, the pitching moment measurements from the fiber optic sensors

were used to calculate the normal force. Normal force (lbs) versus run time (seconds) is shown Figure 4.5. The total stagnation pressure (psi) is provided on the right-side y-axis versus run time. As the stagnation pressure levels out at about the 5-second mark, the average normal force readings for the fiber optic sensors and the foil strain gages are 6.3 lbs and 7.7 lbs, respectively.

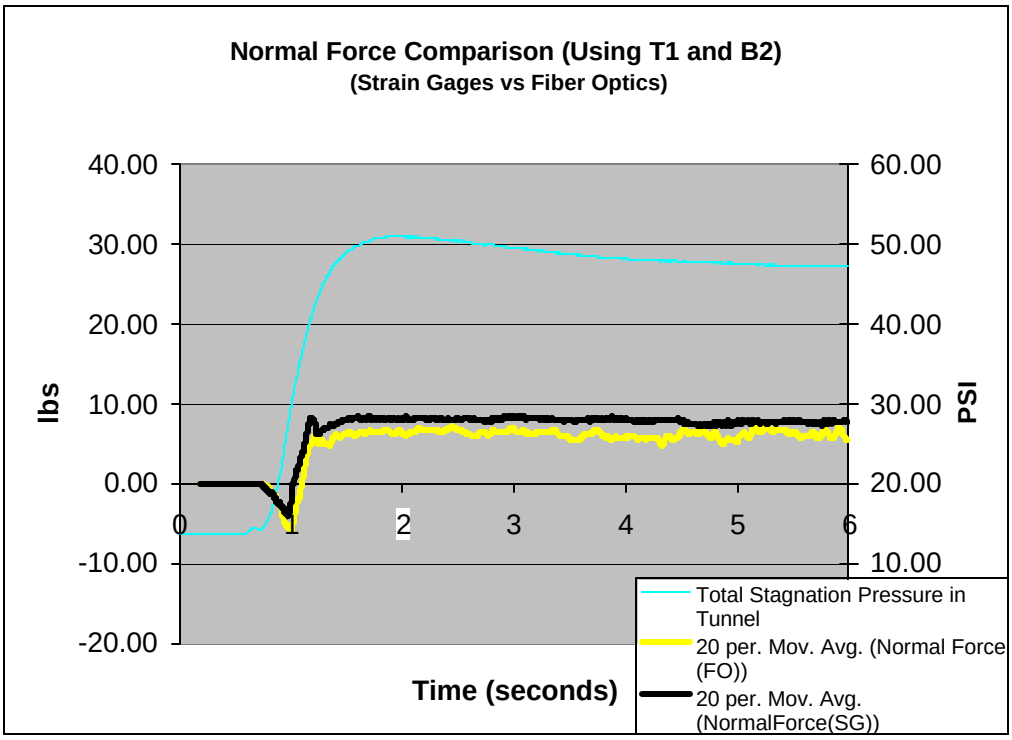

Figure 4.5 - Normal Force Comparison

The pitching moment is then referenced to the base of the cone to compare the actual experimental results to the CFD predictions. Again, pitching moment versus run time is provided with the average readings taken between the 5-second and 6-second mark, as this is where the stagnation pressure in the tunnel approximately reached steady state. The stagnation pressure versus time is also provided in Figure 4.6.

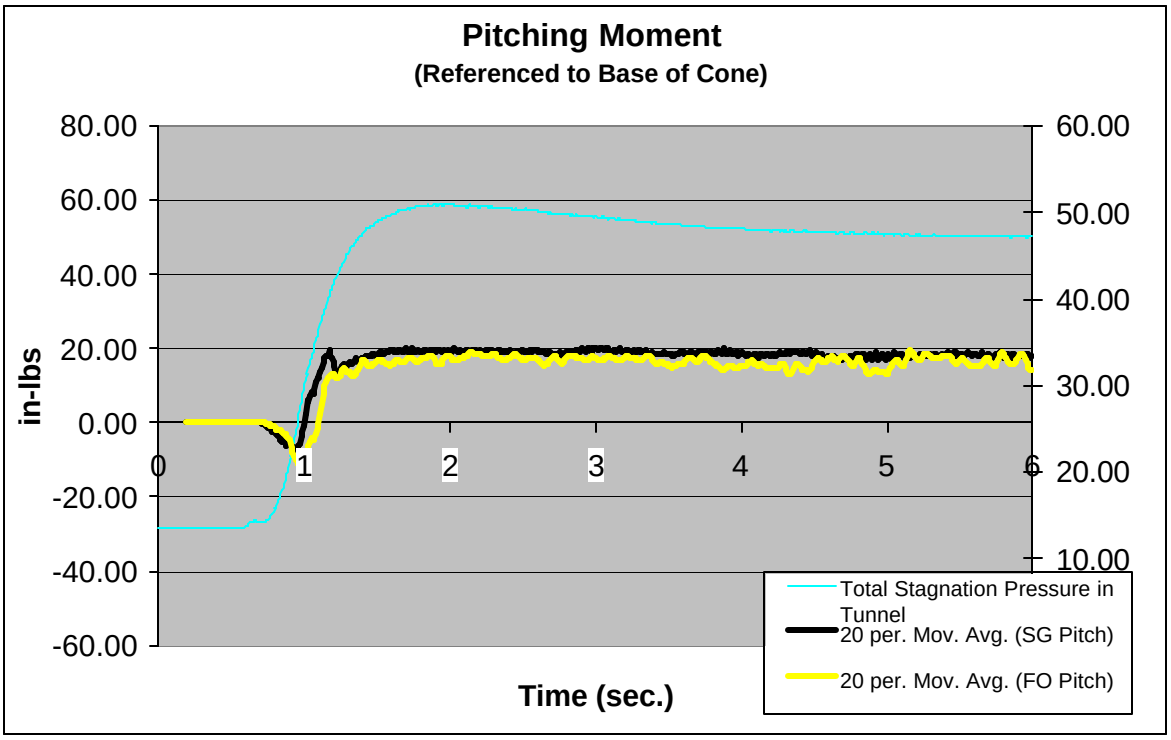

Figure 4.6 - Pitching Moment Referenced to Base of Cone

Overall, the results from the foil gages and the fiber optic sensors were comparable for both the normal force and pitching moments. The calibration process of both sets of sensors could be the cause of the small discrepancy between the measurements from the fiber optic sensors and the foil strain gages. First of all, the calibration for the fiber optic sensors was not as precise as for the strain gages. AEDC routinely performs calibrations of sting balances and therefore has all the proper equipment and personnel for an accurate and precise calibration. Resources at the campus of Virginia Tech for this high-quality calibration procedure were limited, resulting in a less accurate calibration of the fiber optic sensors when compared to the foil strain gages. Another reason for the small discrepancy between the foil strain gage and the fiber optic sensor results could be due to the interaction matrices. Originally, it was assumed that there was no induced side force or yawing moment on the model in the test section. If a small side force or yawing moment was actually produced, this could influence the pitching moment readings.

The actual data also compared favorably to the predictions made by the CFD software. Table 4.2 shows the breakdown of the readings and the CFD solutions. The direct comparison provided in Table 4.2 shows that the fiber optic pitching moment result of 16.8 in-lbs is closer to the CFD prediction of 11.8 in-lbs than the foil strain gage results, which measured 18.2 in-lbs of pitching moment. On the other hand, the foil strain gage normal force results are only slightly closer to the CFD predictions than the fiber optic results.

Average Results for:	*CFD Predictions*	*Foil Gage Results*	*Fiber Optic Results*
Pitching Moment (Ref. To Base of Cone)	***11.8 in-lbs***	***18.2 in-lbs***	***16.8 in-lbs***
Normal Force	***7.1 lbs***	***7.7 lbs***	***6.3 lbs***

Table 4.2 – Comparison of CFD Predictions to Experimental Results

One reason for the discrepancies between the CFD predictions and the actual results could be due to actual change in AOA during tunnel operation. Although the AOA determined from the shadowgraphs was measured in great detail, even a small change in AOA at Mach 2.4 could produce a large discrepancy between the normal force and pitching moment measurements.

A brief uncertainty analysis for both the foil strain gages and the embedded fiber optic sensors are currently being performed and will be included in the final paper.

Chapter 5 – Conclusions and Future Work

5.1 Conclusions

A sting balance was developed for measuring forces and moments during wind tunnel testing using embedded EFPI-based fiber optic sensors. The following conclusions can be reached from this study:

1) A sting balance was developed to measure the normal force and pitching moment of a cone model at Mach 2.4 using fiber optic sensors.
2) Assuming the foil strain gages on the AEDC balance provided the actual forces and moments encountered, comparisons of the foil strain gage and fiber optic sensor measurements were developed and found to be within 8% and 18% for the pitching moment and normal force, respectively.
3) Measurements for the normal force and pitching moment by both sets of sensors were also compared to detailed inviscid CFD calculations. Comparisons of the foil strain gage measurements and CFD predictions were developed and found to be within 35% and 8% for the pitching moment and normal force, respectively.
4) A problem was encountered when applying the fiber optic sensors to the balance in that it was difficult to run the fiber optic leads over the balance and out of the tunnel. This was especially due to the bending constraint on the fiber optic leads.
5) The Finite Element Model (FEM) provided accurate stress results within 5% of the strain gage readings and was an effective tool in choosing the fiber optic sensor locations.
6) The harsh environment encountered during supersonic wind tunnel testing proved to be too unsteady for accurate and precise results. This is evident when compared to the accuracy and precision found during the load cycle

tests performed by Luna Innovations, Inc. Both the fiber optic sensors and the foil strain gages measured this unsteadiness equivalently.

Although some of the fiber optic sensors were found to give inaccurate results, this was mainly due to the calibration procedure. Both sensors may have been accidentally hit during this procedure, causing the sensors to either stop working properly or stop working entirely. The two sensors that were used to calculate the pitching moment and normal force were again calibrated after the testing and found to be still working properly. After referencing the pitching moments to the fiber optic locations, it was also shown that fiber optic sensors T1 and B2 were giving accurate results. Therefore, the results obtained by these sensors were both reliable and accurate. Overall, this was a successful first trial application of fiber optic sensors on a sting balance in a supersonic wind tunnel.

5.2 *Future Work*

The application of fiber optic sensors on a sting balance provides numerous potential advantages such as increased accuracy and resolution, insensitivity to EMI, and use at high temperatures. Therefore, future work in this area should be towards designing and developing an entirely new sting balance only equipped with embedded EFPI-based fiber optic sensors. The designer should take advantage of the most favorable characteristics of fiber optic sensors by creating a sting balance that is smaller, cheaper, and easier to machine, while keeping the accuracy and precision of today's conventional high-performance balances.

References

[1] Harper, J.J., and Pope, A., "Model force, moment, and pressure measurements," *Low-Speed Wind Tunnel Testing*, John Wiley & Sons, New York, 1966.

[2] Volluz, R.J., "Handbook of Supersonic Aerodynamics, Section 20, Wind Tunnel Instrumentation and Operation," NAVORD Report 1488, Volume 6, January 1961.

[3] Carlson, B.A., and Gisser, D.G., "Resistive Circuits," *Electrical Engineering Concepts and Applications*, 2nd ed., Addison-Wesley Publishing Company, New York, 1990.

[4] Fuhr, P. L., "Part 2: Fiber-Optic Sensing—From Theory to Practice," Sensors, May 2000.

[5] Pulliam, W. J., "Development of Fiber Optic Aerodynamic Sensors for High Reynolds Number Supersonic Flows," PHD Dissertation, Virginia Tech.

[6] Pulliam, W.J., Russler, P.M., "Developments in Fiber Optic Sensor Technology for Harsh Environments," Luna Innovations, Inc., Blacksburg, VA.

[7] Borinski, J., "Phase I Final Report: Fiber Optic Sensor Development," Luna Innovations, Inc., Blacksburg, VA.

Vita

Alexis Timothy Robertson Edwards was born in Kalamazoo, Michigan on March 16, 1977. He graduated with a Bachelor of Science Degree in Aerospace Engineering from Virginia Tech in May of 1999. He then continued on at Virginia Tech and received his Master's Degree in Aerospace Engineering in December of 2000 where he gained valuable design and testing experience in the field of aerospace engineering.